BEN- GURION UNIVERSITY OF THE NEGEV
THE FACULTY OF NATURAL SCIENCES
DEPARTMENT OF GEOLOGY

EVOLUTION OF SURFACE ROUGHNESS THROUGH SHEAR

THESIS SUBMITTED IN PARTIAL FULFILLMENT OF THE REQUIREMENTS FOR
THE MASTER OF SCIENCES DEGREE

Submitted by
GUY DAVIDESCKO

This work has been conducted under the supervision of
Prof. Yossef H. Hatzor, Ben-Gurion University of the Negev, and
Dr. Amir Sagy, Geological Survey of Israel

3/2013

BEN- GURION UNIVERSITY OF THE NEGEV

THE FACULTY OF NATURAL SCIENCES

DEPARTMENT OF GEOLOGY

EVOLUTION OF SURFACE ROUGHNESS THROUGH SHEAR

THESIS SUBMITTED IN PARTIAL FULFILLMENT OF THE REQUIREMENTS FOR

THE MASTER OF SCIENCES DEGREE

GUY DAVIDESCKO

Signature of student: _____ Date: _____

Signature of supervisor 1: _____ Date: _____

Signature of supervisor 2: _____ Date: _____

Signature of chairperson

Of the committee for graduate studies: _____ Date: _____

3/2013

Abstract

Fault zones in the upper crust contain discreet principal slip surfaces which are generated by shear and absorb the majority of the fault displacement. The topography of these surfaces is integral to earthquakes and fault mechanics but is practically unknown. We shear matching rough tension cracks in a Direct Shear System to distances varying from 5 to 15mm, scanning them using a laser profilometer before and after shear in order to isolate the effect of shear on surface roughness and characterize the relationship between shear distance and surface roughness. The results demonstrate that roughness decreases under shear and that the sheared surface is polished as a function of slip distance. The amount of surface polishing as a function of measuring scale is not trivial. We find that at large scales the roughness is decreased by a constant ratio, whereas smaller scales are less affected. Our interpretation is that the asperities fracture and yield during shear, although never by total decapitation. Thus large scales are affected proportionately to their size. On the other hand, we also observe that under the conditions applied in our experiments, small scale polishing is less effective, probably due to dilation during shear. A decrease in roughness of each scale proportionate to its size is expected to have a strong effect on resistance to shear and gouge generation of natural faults.

Special Thanks

I would like to begin with a few words to the people that helped me throughout my research.

To Dr. Eran Sharon and Dr. Gil Cohen of The Racah Institute of Physics, The Hebrew University of Jerusalem, I want to give thanks for welcoming me to your lab, teaching me how to use the relevant equipment for my research and for helping me with any problem I presented to you.

To Dr. Dorit Korngreen of the Geological Survey of Israel, I want to give thanks for your devoted work on the professional analysis of thin sections.

To Omer Biran and Dr. Dagan Bakun-Mazor, I want to give thanks for taking the time to teach me how to use the Direct Shear System.

To Dr. Vyacheslav Palchik of Ben Gurion University of the Negev, I want to give thanks for helping me perform Uniaxial, Brazilian and sonic tests.

To Prof. Yossi H. Hatzor of Ben Gurion University of the Negev, I want to give thanks for taking me under your wing, believing in me, teaching me allot of Geology and responsibility and for being there when I needed advise.

To Dr. Amir Sagy of the Geological Survey of Israel, I want to give thanks for all your encouragement whenever I was a little lost, all the time you spent teaching me all the aspects of research and for your passion for my research that excited me every time.

Table of contents

Figures

Chapter 1: Introduction

1.1 Fault topography in relation to slip history

Fault zones in the upper crust contain discreet principal slip surfaces which are generated by shear and absorb the majority of the fault displacement (Sibson, 1977; Chester and Chester 2000, Ben Zion and Sammis 2003). All movements of one brittle surface against another, particularly of matching rock surfaces, generate wear. The wear is the result of the partially or completely broken asperities (Archard 1953) and its generation is probably an essential factor that shapes fault topography (Sagy et al., 2007).

Fault topography is one of the major determinants of slip distribution in an earthquake (Parsons, 2008). It strongly affects resistance to shear (Wang and Scholz, 1994), critical slip distance (Ohnaka 2004), fault dynamics (Dunham et al., 2011), fault gouge generation (Power et al., 1988) and near-fault stress fields (Dietrerich and Smith, 2009; Sagy and Brodsky, 2009; Griffith et al., 2011). Pioneer works on slip surface roughness based on contact profilometers suggested that the geometry of fault surfaces is fractal (Power et al., 1987; Power et al., 1988; Power et al., 1991). Recent studies based on optic measurements (Renard 2006, Candela 2011) proposed that a universal power-law characterizes fault surface roughness along a large range of scales (from 0.1mm to a few kilometers). It is however unclear if such roughness characteristics are a natural effect of friction and wear, and how slip surfaces evolve as a function of slip distance and along different scales. The main goal of this study is to investigate these issues using accurate optical profilometer measurements and controlled laboratory direct shear tests as described next.

1.2 Research goals

Field measurements of natural faults pointed to an evolution of fault roughness as a function of slip (Sagy et al., 2007). Quantifying the process is however difficult due to the varieties in lithologies and tectonic environments which affect wear, as well as processes of cementation and erosion that affect any exposed surface in the field (Brodsky et al., 2011). We therefore believe that adopting an experimental approach might be the best strategy for isolating parameters that affect surface roughness. While the process of wear accumulation has been studied in detail during the last century (e.g Archard 1957, Qweener 1966, Levy and Jee., 1988; Power et al.,

1988; Kato and Adachi, 2000, Wang end Scholz, 1994), the effects of wear on roughness evolution of rock surfaces has been only partially studied in laboratory experiments (Wang end Scholz, 1994; Chen et al., 1993), despite its great importance for understanding slip on natural faults, assessing seismic risks, and earthquake modeling. The objective of the current research is to measure and characterize the evolution of slip surface topography as a function of shear distance along a range of length scales.

Characterization of the dependence of the roughness profile, at different scales, on the amount of slip can help understand the evolution of roughness in natural faults. It can also be an indicator for the amount of slip on natural faults associated with faulting activity. Furthermore, the comparison of the roughness profile at different scales and magnitude of shear displacement will help test the validity of the universal power law proposition discussed in Sec. 1.1 and to clarify if the suggested power law is only a result of slip, or if it incorporates other effects (e.g cementation, unloading and surface erosion).

1.3 Research scope

The present research is focused on experimental assessment of fault surface evolution in light of the assumption that friction and wear are fundamental and interrelated mechanisms for this process. Shear experiments in rocks are usually conducted by shearing one surface against the other (Byerlee 1978), or by fracturing a single intact sample and then shearing the generated fracture in one continuous test segment (Chen et al., 1993). Here a slightly different approach is taken: we begin by fracturing a single prismatic block in tension using three hinged beam tests, and then shear the obtained fracture surface in direct shear keeping the original fracture surfaces in a perfect matching configuration. We chose this alternative because the initially matching surfaces better simulate natural faults before slip initiation (Segall & pollard 1983). Furthermore, by adopting this experimental procedure the surface morphology can be measured before and after shear displacement while variations in roughness can be examined between different shear distances and at different scales. Due to constraints associated with the direct shear assembly, the slip distances we study in this research program are relatively small; they vary between 5 to 15 mm. The pre and post roughness changes in profiles were compared between different scales and different shear distances.

Chapter 2: Scientific Background

2.1 Fracture Roughness

The roughness of fracture surfaces has been studied in great detail during the past several decades. Mandelbrot et al. [1984] were first to report that geometry of fractures in metals between microscopic (grain size scale) and macroscopic dimensions (sample scales) can be describe by fractal hierarchy, regardless of the experimental conditions. This observation triggered countless research papers which suggested that fracture topography and roughness are best described by fractal geometry. Fractal geometry means that the studied object is scale invariant and displays similar patterns along a wide range of scales. The relationship between the geometry and the different scales can be defined by a power law if it is indeed fractal. Repeatedly determined dimensions of different fractured samples of the same materials have often resulted in identical values and this has led some authors to the idea of a universal co-dimension, $\zeta = 0.8$, that characterizes tensile fracture surfaces as a whole (Bouchaud et al., 1990). This idea, however, still invokes certain doubts (Carpinteri et al., 2000).

2.2 Fault roughness

Natural joint and fault roughness were measured by Brown and Scholz (1984) which demonstrated scale dependence roughness (e.g non-fractal roughness).

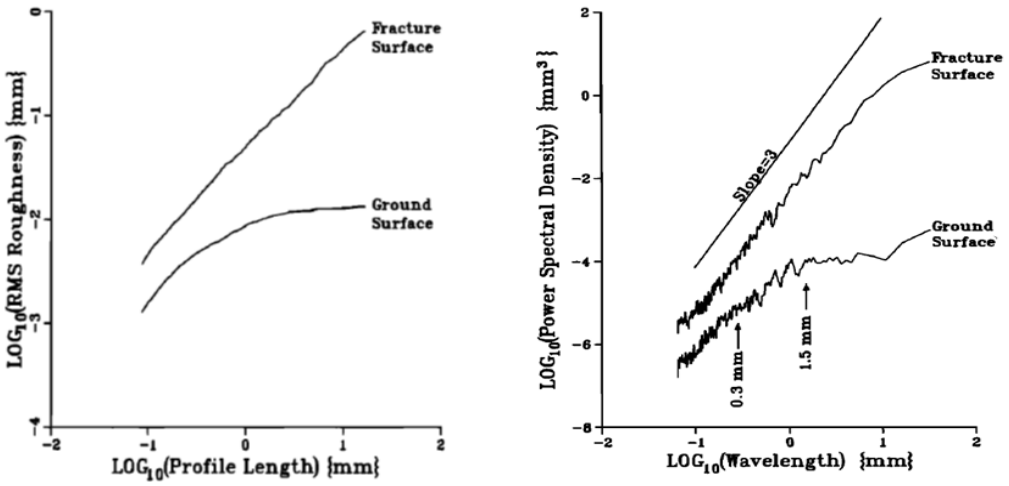

Figure 1: : Root Mean Square of a fracture and a ground surface as a function of observed profile length (left), power Spectral Density of a fracture and a ground surface (right). In this example the ground surface has a constant RMS if the observed profile is longer than 1.5mm while the RMS of the fracture doesn't have a constant RMS value. Modified from Power et al., 1988.

Power at all (1987, 1991) were the first to suggest, however, that natural fault surfaces are rough in all measurable scales (Fig. 1). Moreover, they also suggested that the average deviation of the topography from a planar surface, the Root Mean Square roughness, (eq. 1) parallel and perpendicular to a striated slip surface is scale-invariant, or self similar. If a surface is self similar, a small portion of the surface, when magnified isotropically, will appear statistically identical to the entire surface (Power et al., 1991).

1) $X_{rms} = \sqrt[2]{\frac{1}{n}(x_1^2 + x_2^2 + \cdots + x_n^2)}$

The roughness profile can also be presented using power spectral density (PSD). The PSD measures the strength of the sinusoidal components of the topography height over a range of wavelengths by performing Fourier decomposition (Fourier series decomposes periodic

functions or periodic signals into the sum of a set of simple oscillating functions, namely sines and cosines, Power et al., 1988; Brodsky et al., 2011).

Following Brodsky et al.,(2011), the PSD function is mathematically identical to RMS for the special case in which the topographical data in spectral space can be fit by a power law of the form:

2. $p(k) = ck^{-\beta}$.

Where c is the material constant and β is the slope of the PSD function. The RMS height H of a profile y(x) over a segment of length L is related to the spectral power density by Parseval's Theorem as:

3. $H = (\frac{1}{L}\int_0^{-L} y^2(x)dx)^{\frac{1}{2}} = (\int_{1/L}^{\infty} p(k)dk)^{\frac{1}{2}}$ (George et al., 2001)

If 1<β<3 for a section of length L substituting eq. (2) into eq. (3) yields, after simplifying:

4. $H = \sqrt{\frac{p(\lambda=L)L^{\beta-2}}{(\beta-1)}}$

Renard et al., 2006 used optical profilometers and Lidar to measure slip surface geometry and used PSD analysis and wavelength analysis to show that fault surfaces are self affine (anisotropic self-similarity) with typical power of 0.8 perpendicular and 0.6 parallel to the slip direction. Candela et al., 2011 added validations to the power law established by Renard using models that predict the influence of fault roughness on frictional strength under the assumption that the origin of the spatial fluctuations in frictional strength along faults is due to the elastic deformation of fault asperities; they suggested that self-affine geometrical properties of fault surface roughness control slip correlations and that a typical power of 0.6 fits a wide range of faults parallel to the slip direction.

Recent results reported by Sagy and Brodsky., (2009) and Griffith et al., (2011) suggested scale dependence variations in profiles parallel to the slip direction, and moreover, that one power law cannot describe the entire surface roughness data obtained from several natural faults as measured in the field.

Another important recent observation is that fault roughness evolves with slip towards geometrical simplicity (Fig.2). Sagy et al., (2007), and Sagy and Brodsky (2009a) observed that faults that accommodated a relatively large slip distance (tens to hundreds of meters) are smoother, for every measurable scale parallel to the slip orientation, in comparison to small-slip faults (centimeters to few meters of slip). Interestingly, large quasi elliptic bumps with wavelength greater than 10 m parallel to the slip direction were observed on relatively polished surfaces of several large-slip faults. In these faults, the smaller scales were found to be more affected by slip than the larger scales. These observations suggest that the effect of slip on surface roughness is scale dependent. On the other hand, faults that have undergone only small amount of slip will exhibit asperities over the entire range of observed scales.

Fault striations are generally attributed to wear processes. Sagy and Brodsky (2009b) hypothesized that wear in the upper crust may change the fault geometry through the faults' history, thus affecting the fundamental earthquake characteristics. Moreover, since the difference between a large and damaging earthquake and a small, inconsequential one is simply the continued propagation of slip, understanding the role of a resistance process like wear is crucial to developing a physics-based model of earthquake damage. Thus, a quantitative measure of the degree of wear with slip is necessary for modeling fault surface geometry and its evolution with slip.

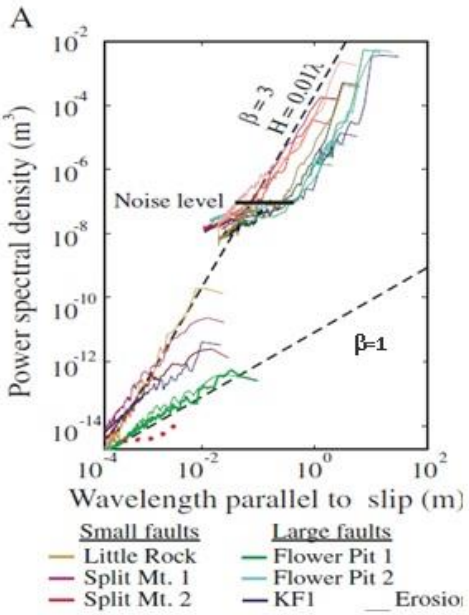

Figure 2: Power Spectral Density as a function of wavelength of large and small slip faults. The slope (β) determines the relationship between The PSD values and the sample length. The smaller wavelengths show a significant drop in the slope (from sagy et al., 2007).

Direct wear measurements on natural faults are tricky, mostly because it is difficult to separate wear products from other types of damage in the fault zone and because wear does not directly imply a change in surface topography. An alternative approach to learning about fault topography is by measuring fault roughness. Fault roughness is a particularly rich source of information. Continuous slip should have measurable effects on a fault surface that can be captured and quantified through careful measurement of the roughness at different scales. Power et al., (1988) were the first to use fracture roughness data for the study of wear processes in natural faults, their roughness measurements were based on a contact profilometer. This method is labor intensive, so only a few profiles were reported for each surface. Renard et al. (2006) began to increase the amount of data sets by examining a fault surface with ground-based LiDAR. Sagy et al. (2007) went further by comparing multiple faults and adding laboratory profilometer data. The comparative data of Sagy et al. (2007) and Sagy and Brodsky (2009) established that fault surfaces are smoothed by successive slip events, thus providing a hint for answering the fundamental question of the role of wear in fault physics.

2.3 Wear of rocks: Concepts and experimental observations

While the information about surface roughness and wear processes in natural faults is limited, laboratory experiments supply extensive data and analyses of the inter-relationships between roughness, wear and friction. The basic model for wear between sliding solid brittle blocks was developed by Archard (1953), and was later extended by Qweener et al., (1965). The model assumes that wear occurs at the real contact area between the solid blocks, which is significantly smaller than the nominal area. Queener et al., (1965) have shown in their experiments of rough surfaces that during shearing, wear production has two phases (Eq. 5). In the first phase, named transient or running-in wear, most wear materials are formed. Transient wear destroys the initial surface irregularities and leads to the development of the second phase – steady state wear. Once steady state has developed wear proceeds at a much lower rate (figure 4).

5. $V = A(1-\exp(-K_1 x) + K_2 \frac{\sigma_n}{H} x$

Where V is the produced wear volume, A is the average roughness, x is the slip distance, $K_{1,2}$ are constants, σ_n is the normal stress, H is the stiffness of the softer component. It is important to note that Eq. 2 suggests that roughness is only directly affecting the transient wear.

Patton (1966) demonstrated experimentally that natural surface roughness has a significant influence on its shear behavior and strength under relatively low normal stress levels, of interest mainly for civil engineering applications. Patton showed that under low normal stress levels the roughness profile directly affects shear strength with the roughness angle added to the friction angle of an otherwise smooth surface, thus defining the "dilation angle" which, together with the basic friction angle of smooth surfaces, provides the ultimate, or peak, friction angle of rough surfaces. Under high normal stresses, however, Patton showed that the mobilized friction angle of the sheared surface degrades back to the basic friction angle of smooth surfaces. These experimental findings of Patton were formulated in the classical Bi-linar failure criterion that has been typically named after him. Patton's results are very relevant to civil engineering applications where the level of normal stress is not expected to exceed several MPa's. In seismological and geophysical applications, however, under high normal stress levels associated with natural faulting, the strength of the intact asperity material is exceeded by the developed shear stresses across the shear surface and the asperities tend to be sheared through during slip

(figure3) (Barton, 1973, 1976; Byerlee, 1978), thus developing surface wear with onset and propagation of slip.

Experimental observations under laboratory conditions of slip along pre-existing surfaces under normal stresses demonstrated that wear loss, as a function of displacement, is similar for many materials and configurations (Wang end Scholz, 1994, Queener et al. 1965).

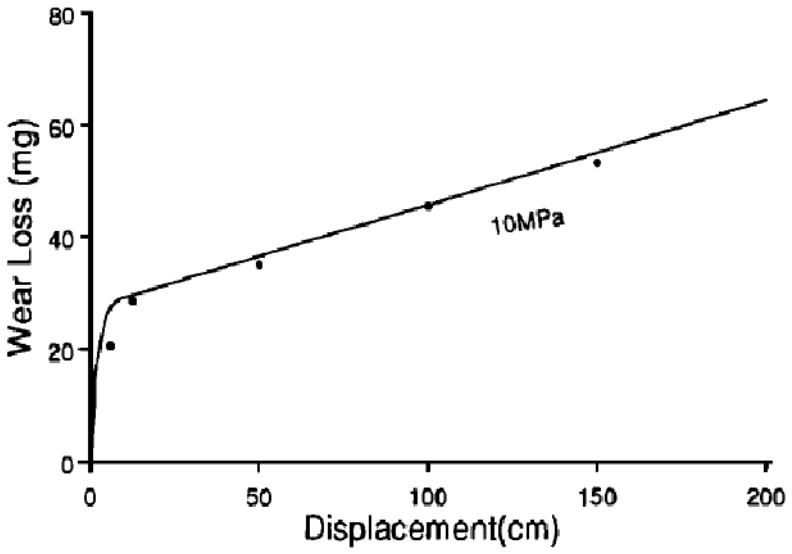

Figure 3: Wear loss as a function of displacement, high rate at transient phase and lower rate at steady state phase (Wang and Scholz, 1994).

Power et al., (1988) have shown in their roughness measurements on artificial fractures that their obtained roughness profiles are self similar, namely that the root mean square of roughness increases in proportion to the scale of observation (Figure 1). They concluded that in contrast to experimental faults that have a finite roughness, slip on natural faults isolates progressively larger irregularities from their original position in the opposite surface, causing wear to occur in an increasingly thick zone. They have also suggested that wear zone thickness of natural faults depends linearly on displacement because the size of the asperities that must be broken increases with an approximately linear relationship to displacement (Figure 4).

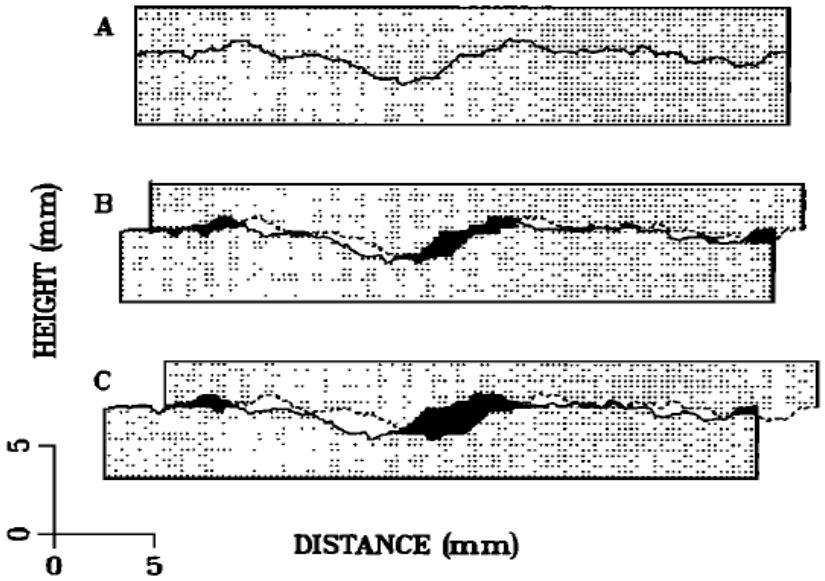

Figure 4: conceptual model for wear of a matched fractal fault (Power et al., 1988)

However, the amount of wear produced during the sliding of the surfaces against each other does not provide information as to how the roughness has evolved after a certain amount of slip. In order to better understand how the topography of a natural fault is affected by slip it must be measured directly.

Brodsky et al., (2011) presented direct field measurements of fault surfaces roughness and found that the smoothing rate (RMS decreasing as function of the slip) in the field is correlated to $X^{-1.1}$ where X is the total displacement. They used this observation for modeling the effect of wear on fractal fault surface and found that wear accommodation rates as function of slip distance, dV/dX is correlated to X^{-1}.

2.4 Roughness evolution of shear fractures

There is little experimental data on the evolution of roughness as function of slip, and empirical equations such as equation 2 still have not been suggested to describe quantitatively the evolution of surface roughness with propagation of slip. It is important to note that there is no trivial symmetry between wear production and roughness evolution. Wear production could theoretically have three different effects on surface roughness: a) it could have no affect at all on the surface roughness provided that for every asperity that is sheared off an equal amount of rock

is removed creating a mirror image on the opposite surface, b) The roughness could increase provided that the mirror image of the asperity is greater that the asperity removed, c) The roughness could decrease in the case that the asperities are sheared off and no mirror image is created or that the mirror image is smaller than the original asperity, resulting in smoothing of the surface.

Chen & Spetzler (1993) have demonstrated in their shear experiments performed on Westerly granites how surface roughness can be affected by the wear process. They measured three profiles from fracture surfaces of originally intact samples. The samples were loaded to shear failure under triaxial loading. After failure the fractures were placed arbitrarily, reloaded and sheared to a certain distance. They observed slope break in the Power Spectra Density versus spatial frequency plots. The slope break in the Power Spectral Density reflects changes in the surface roughness. This observation might support a hypothesis that scale dependence roughness is originated under shear and wear. However the effects of shear distance on surface roughness in these experiments wasn't isolated and the effect of shear distance on different roughness scales could not be determined.

Recently, Renard et al. (2012) presented laboratory experiments where he tracked the morphological and mechanical evolution of an interface during slip. Their laboratory friction experiments consist of a halite (NaCl) slider held under constant normal load that is dragged across a coarse sandpaper substrate. Surface morphology evolution was recorded with cumulative slip. They directly observed the formation of deformation features, such as slip parallel linear striations, as well as deformation products or gouge. Experiments with an abundance of gouge at the sliding interface have reduced shear resistance compared to bare surfaces. They have also characterized the scaling properties of the rough surfaces. The topography shows a self-affine geometry. The different slip surfaces analyzed cover approximately 2 orders of magnitudes of length scales and show a scaling relationship with a Hurst exponent (a dimensionless estimator for the self-similarity of a series) that varies with cumulative slip.

Chapter 3: Methods

Experimental procedure

In this research we used matching tension fractures which have been shown to possess roughness properties of natural faults (Power et al., 1988), and ensured the surfaces in our experiments have not undergone any shear displacement prior to testing. We have sheared several fractures to different distances and then characterized the roughness before and after shear and compared them in order to isolate the direct effects of shear on surface roughness. The following chapter will explain in detail the manufacturing procedure of the artificial tension cracks, the direct shear system used in this research, the procedure used to acquire roughness data and the analysis procedures of the obtained roughness profiles.

In order to test how roughness of a slip surface is evolved as a function of slip distance a series of experiments have been performed in the following stages:

a. Generating a tension crack in the mid section of a continuous, prismatic, limestone beam using the "three hinged beam" testing methodology.

b. Scanning the surface roughness of the obtained tensile fracture using laser profilometer.

c. Re - matching the two surfaces of the tensile fracture after scanning and casting in shear box assembly.

d. Direct shear testing of the matching surfaces under imposed constant normal stress and constant sliding velocity to different shear displacement targets varying between 5 mm to 15 mm.

e. Re - scanning the obtained surface roughness of the tensile fracture after shearing to pre specified displacement target using laser profilometer.

f. Analyzing the evolution of surface geometry as a function of scale and slip distance.

The rock samples we used are fine grained limestone from top Judea Group of central Israel with an average grain size of 0.3 mm and amorphic carbonate cement, from which the prismatic beams were machined for the three hinged beam tests. This starting material was selected

because of its homogeneity and because the grains are relatively small. In addition, it does not have many reflecting features that cause measurement errors when scanned with a laser profilometer.

The experimental procedures used in this research are discussed in detail below.

3.1 Direct Shear system

The direct shear system allows simultaneous application of horizontal (shear) and vertical (normal) forces on two mating rough fracture surfaces using hydraulic pistons. Through direct shear tests the shear strength of intact and fractured rock can be determined. There are a few different types of direct shear system configurations (figure 5).

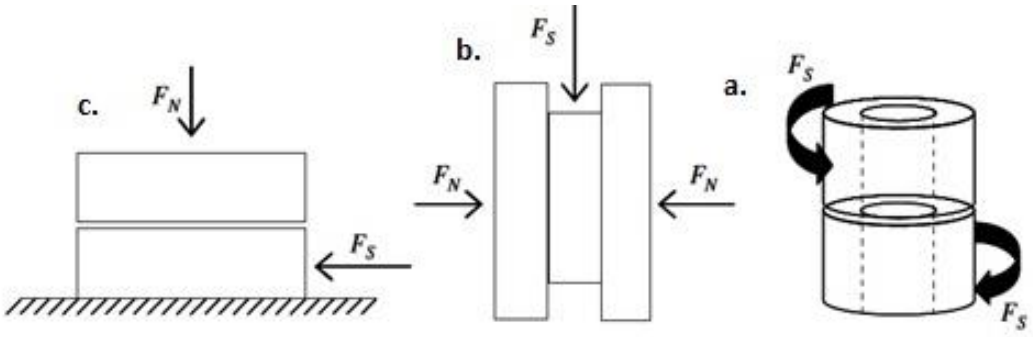

Figure 5: Illustrations of different shear systems. A) Rotary shear test. B) Double shear test. C) Direct shear test. (Jaeger et al., 2007).

The different testing configurations have different piston positions, sample shape, and imposed boundary conditions. Each direct shear testing methodology has its advantages and disadvantaged as a result of the different configuration and boundary conditions.

Direct shear tests have two limitations; 1) the failure surface is pre-determined when testing initially intact rock samples, and 2) the principal stress axes rotate as relative movement begins across the shear interface. The direct shear system at the Rock Mechanics Laboratory of the Negev at Ben-Gurion University is a single plane shear system (figure 6) designed and manufactured by Terratek System Inc, USA (model DS-4250) (figures 7, 8 and 9). The system is composed of four main components:

- Hydraulic pump which provides oil pressure for hydraulic pistons

- Hydraulic pistons in two perpendicular directions (normal and shear).

- Real time closed loop servo controlled system that monitors the displacements, forces and stresses that the pistons apply on the sample

- Real time dynamic data acquisition from all channels and storage.

In a system of this configuration the normal stress is applied from one direction and this can cause uneven normal stress distribution across the tested interface. The influence of this test artifact on the resulting shear behavior however is considered negligible.

Figure 6: A general view of the direct shear system DS-4250 at Rock Mechanics Laboratory of the Negev at Ben-Gurion University

3.1.1 Specifications and technical data of the direct shear system

Hydraulic pistons and shear boxes

Two hydraulic pistons apply forces on the shear boxes simultaneously in perpendicular directions: a normal piston, which applies a force perpendicular to the shear direction and a shear piston, which applies force parallel to the shear direction. The pistons are assembled in a stiff steel loading frame (figure 8).

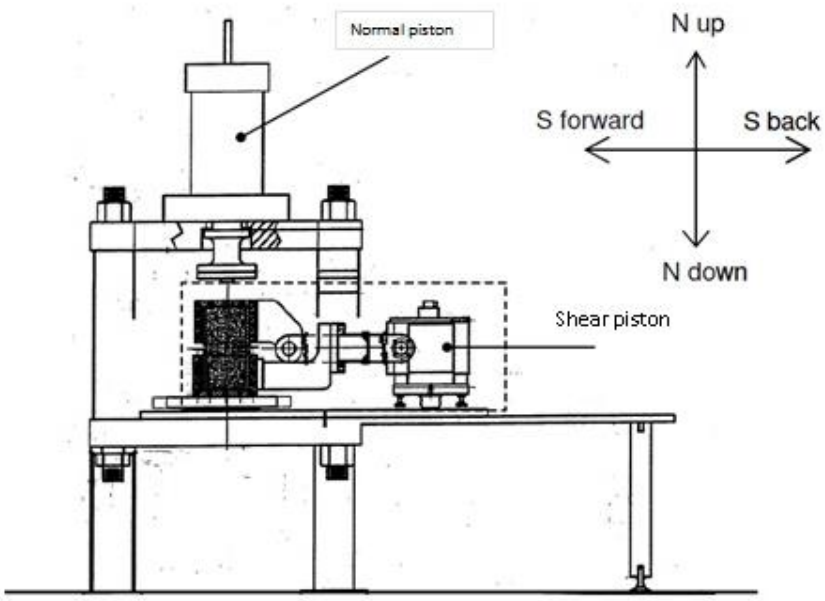

Figure 7: Illustration of the direct shear system: the normal and shear piston inside the load frame. The arrows on the right indicate the directions of movement.

The maximum forces that the pistons can apply are 300 kN and 1000 kN for the shear and normal pistons, respectively. Rock samples are cast into the steel shear boxes using in house made cement. The shear boxes are the components that link the pistons and the rock samples in this experimental system. The shear piston is connected to the lower shear box with bolts, and the normal piston connects to the upper shear box with a centering pin located on the piston so that it fits into a socket located in the middle of the top of the upper shear box (figure 9).

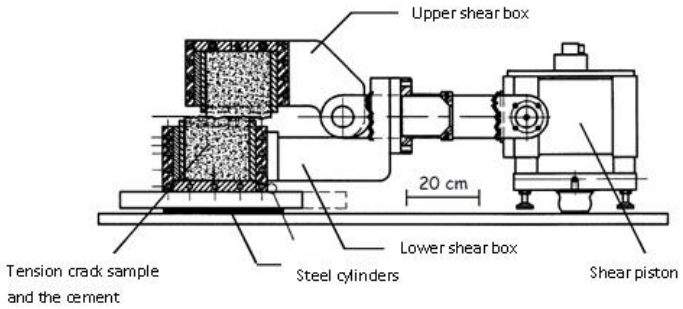

Figure 8: Focus on the shear piston

Applying shear force on the lower block by the shear piston causes relative motion between the lower and upper shear boxes across a pre-determined discontinuity surface (figures 8 & 9). In order to ensure that friction, which is the force resisting the relative motion, is developed only on the pre-determined discontinuity surface between the blocks, the upper block is fixed to the loading frame and the normal piston and the lower block is placed on frictionless rods which are free to roll on the lower platen, thus preventing the development of friction between the block and the lower platen. A big advantage of this particular shear system configuration is the closeness of the displacement transducers (LVDT type) to the interface on which shear is occurring. The very near position of the displacement transducers to the sliding surface greatly improves the accuracy of the measurements and control over the movements of the sample. On the other hand, this configuration limits the target shear distance and the imposed shear velocity (compared with a rotary shear system for example).

Load and displacement measurements

The forces the two hydraulic pistons apply are measured with two load cells located on the pistons near the shear box. The vertical and horizontal movements of the sample are measured with 6 GHSA-750-1000 Linear Variable Differential Transformers or in short-LVDT's placed on the shear boxes; four LVDTS's measuring the vertical movement are placed in each corner of the shear box and two horizontal LVDTS's are placed at the front, parallel to the direction of shear sliding (figure 10). The LVDT transducers are placed on aluminum surfaces fixed to steel frames which are placed inside the shear boxes and inside them are the rock samples.

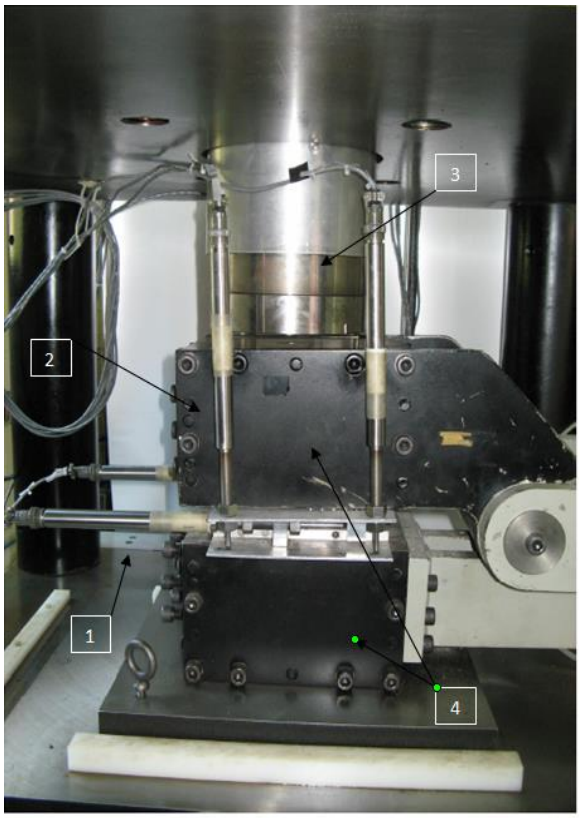

Figure 9: 1) The horizontal displacement transducers 2) The vertical displacement transducers 3) The normal piston 4) The shear boxes. All are assembled and ready for a shear test.

In simple terms, the load and displacement transducers are convertors measuring electrical voltage changes resulting from movements of a spring or a rod located inside the load cell and LVDT transducers, respectively. As a result of shortening or lengthening of the spring or displacement of the rod, the electrical output that the gauge emits to the control unit changes. The volts [V] emitted are converted to engineering units by multiplying the voltage values in each channel by the appropriate calibration parameter. This operation is done automatically by the real time data control and acquisition system. Output values from all channels in both Volts and engineering units are displayed in the control interface. The calibration parameters for every channel were obtained by performing specific calibration for each transducer used in the experiments. An example of a typical calibration chart is shown in (Figure 11). In addition to the calibration parameter the calibration charts also provide estimation of the linearity of the calibration, determined by fitting a linear trend line through the calibration data points. The GHSA-750-1000 displacement transducers are capable of measuring maximum displacement of

50 mm with a linearity of less than 0.25% full scale, namely a measurement resolution of less than 0.6µm.

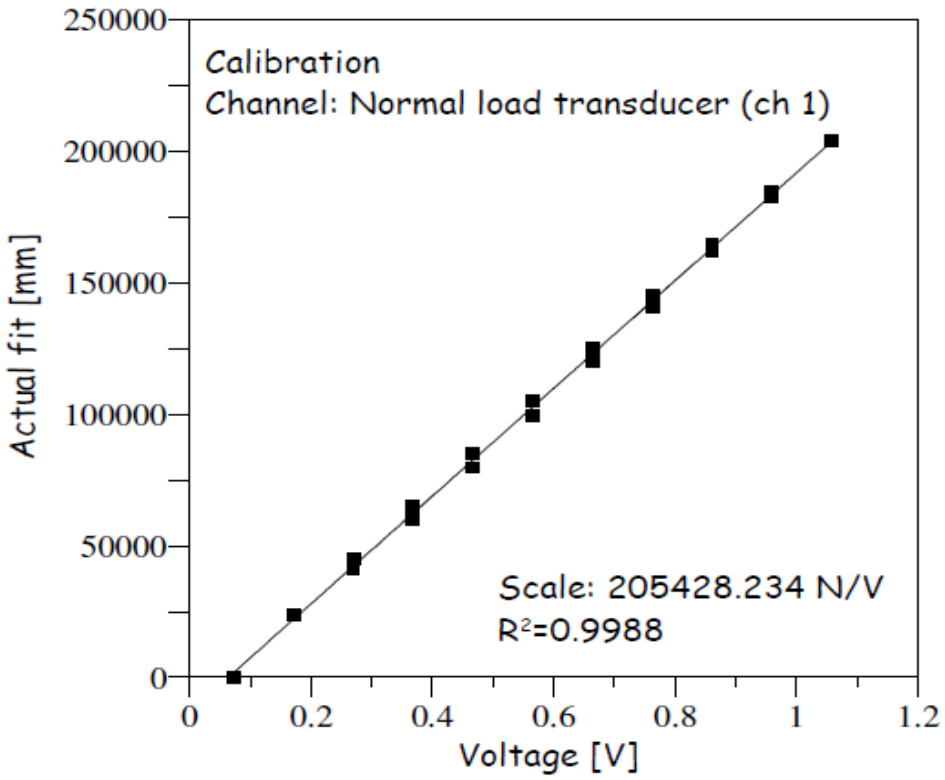

Figure 10: An example of calibration of the normal load cell.

Real time monitoring and control

The monitoring and control system we use in this research were developed by TerraTek Inc., software version Terra TEST V 7.2. The computer control system consists of two computers, "Terra Test Real Time (TTRT)" and "User Interface (UIC)", connected in series by a fast communication cable. The TTRT computer monitors, stores and processes the data; the UIC collects the data and displays it in the user interface. The TTRT computer has a NI REALTIME 8176 RT controller card, capable of receiving and processing 16 different channels at 16 bit resolution. The control rate is 300µs, the data acquisition rate depends on the control channel and varies between 20Hz to 4000Hz. During a test the control interface on the UIC computer displays the data (forces, stress and displacements) in graphs and numerical values. The control panel is separated into two different independent circuits- a horizontal circuit (shear) and a

vertical circuit (normal). Through the control interface each circuit can be controlled separately. Data acquisition rates, for both circuits, can also be determined in the control interface to suit processing needs. Each circuit has a few control parameter options:

Vertical circuit	**Horizontal circuit**
Piston displacement control	Piston displacement control
LVDT vertical transducer control (average of 4 vertical LVDT outputs)	LVDT horizontal displacement (average of 2 horizontal LVDT outputs)
Normal Load control	Load control
Normal Stiffness control	

When determining control mode for a specific channel, relevant control mode, goal, and target parameters for that channel must be entered (displacement control, shear distance and shear rate for example). The pistons will react in such a way that the predetermined goal and target will be reached through the specified control mode. Technically, the input signals will come from the chosen control channel and the piston positioning correction will be performed according to that channel. All the direct shear tests in this research program were performed under constant load in the normal piston, or vertical circuit (constant normal stress), and constant displacement rate (from the average of the two horizontal LVDT's) for the shear piston (the horizontal circuit).

3.1.2 Data acquisition frequency

Test data from all channels are sampled and stored by a dynamic, high frequency, data acquisition system on the UIC. Sampling rate can be modified, by the user, in ranges from 1Hz to 10Hz. The highest sampling rate is much lower than the data collection acquisition rates for monitoring and control of piston movements. Sampling rate is a function of the amount of available system memory for data storage, CPU processing speed and operating system definitions. In the case of 10Hz rate, CPU processing speed is not a limiting factor because the CPU speed is much faster than the sampling speed. In order to measure as accurately as possible, sampling speed should be much faster than the test duration. When shear speed is high, the test

duration is short. Therefore in order to get a sufficient amount of data the data sampling frequency must be high. All experiments were performed at an imposed shear rate of 50 μm/s which is half of the maximum shear rate dictated by the maximum data sampling frequency of 10Hz.

3.1.3 Calibration and quality control of load and displacement gauges

Direct shear experiments examine changes of first and second order in the friction coefficient. Because the changes examined are small (±0.1-0.3), the measurement error allowed by noise has to be very small. To insure that, a calibration of all the gauges was performed as described in chapter 3.1.1.

The purpose of this examination is to test the electrical noise, the gauges deviation and the calculation of the program (stresses and movement averages for example). In addition, this test is meant to validate that in a static state the gauges don't indicate movement. During this test the entire system is assembled as it would be when ready for an experiment. The control system is activated without the hydraulic pump. In this state a real time monitoring of gauges movements is performed. Figure 12 displays an example of such a test on the horizontal displacement transducers (Ya, Yb) and their average (Yave). It is clear that the transducers do not indicate any movement and the inherent electrical noise is smaller than the measurement range (>1exp-3).

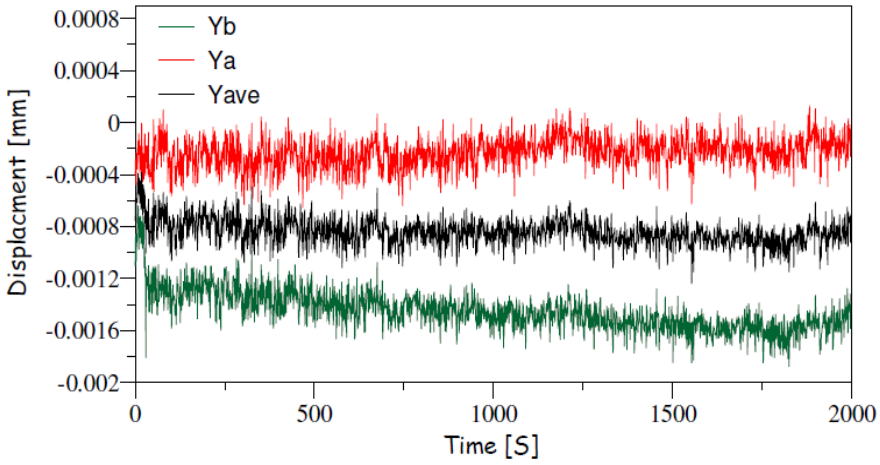

Figure 11: An example of a static test of the horizontal gauges and their average.

3.1.4 Tests output and shear test data processing.

The data file

The data file received after the test is completed contains three types of data:

- General data such as calibration constants during the test, type of measuring units used and the sample area.

- Data that was entered in the user interface: start time, control channels for each circuit, speed, target ranges, monitoring data and data collecting frequency.

- The measurements data which are the main component of data. This data includes both data measured directly from the gauges and data calculated automatically by the software. The details of the data received are displayed on figure 13.

For the most part, the data processing was done graphically. Irrelevant sections such as initial loading were omitted. (You can omit the table below).

	Channel	Sign
measured	Time since test began	Time
	Vertical load cell	Fx
	Shear load cell	Fy
	Shear piston displacement gauge	Sy
	Vertical piston Displacement gauge	Sx
	Displacement gauge-shear	Ya
	Displacement gauge-shear	Yb
	Displacement gauge-vertical	Xa
	Displacement gauge-vertical	Xb
	Displacement gauge-vertical	Xc
	Displacement gauge-vertical	Xd
Calculated	Horizontal displacement gauges average	Yave
	Vertical displacement gauges average	Xave
	Shear sterss	Ty
	Normal stress	Sigx

Figure 12: Detailed data measured and calculated found in the output data file.

3.4 Manufacturing artificial tension cracks for shear testing

The surfaces used in the shear experiments were artificial tension cracks manufactured in "three hinged beam" tests performed at the Rock Mechanics Laboratory of the Negev at Ben-Gurion University. In order to create these tension cracks prismatic beam shaped limestone blocks were purchased and machined to the following dimensions: 55 cm long, 8 cm thick and 15 cm high. These rock beams were placed during a test on two cylindrical steel bases in niches carved into the beam, to prevent the beam from moving during the test. Then the normal piston presses down on the beam, the force is transferred to the beam through another cylindrical steel element placed in a niche carved in the top center of the beam (figure 6).

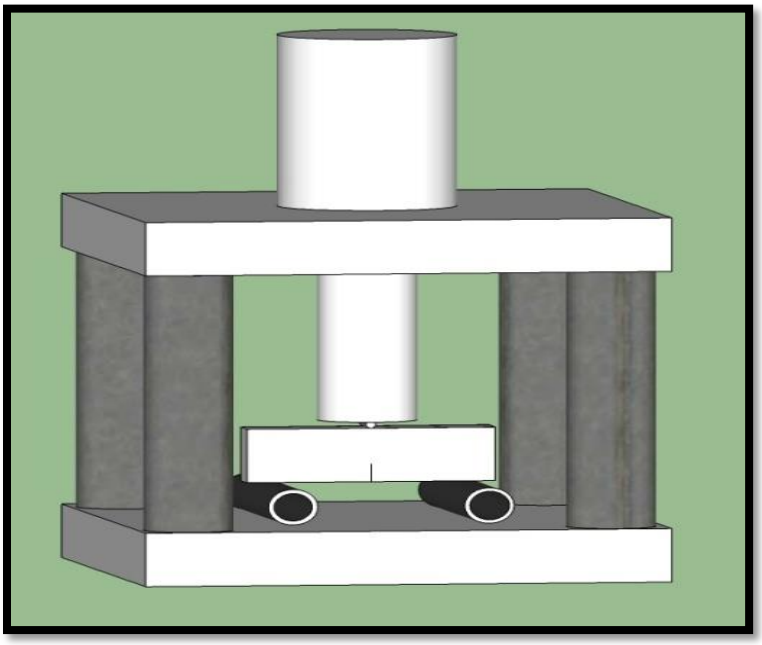

Figure 13: A schematic of the three hinged beam configuration.

An initial crack was curved directly below the applied normal force axis. The initial crack is made in order to ensure that the tension crack is formed at the same orientation as the initial crack. This orientation is also the direction of shear so it is important to ensure that it will be perpendicular to the piston pressing down on it (figure 7).

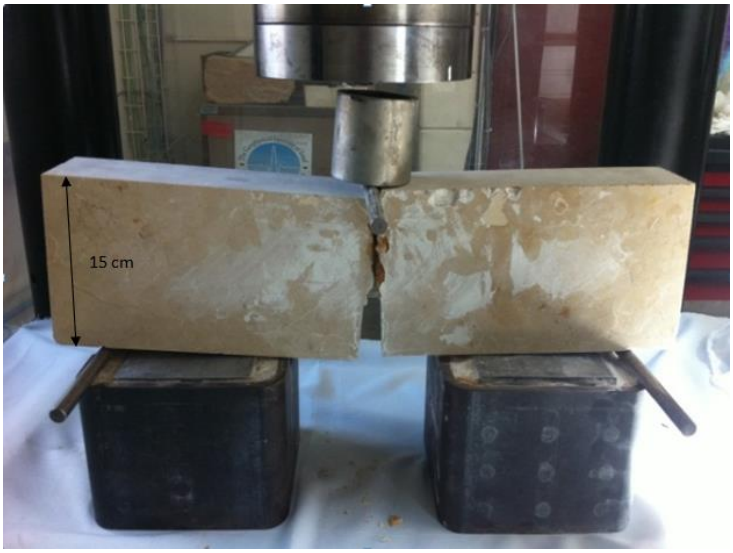

Figure 14: A tension crack manufactured in a three hinged beam test

3.5 Preparation of samples for shear experiments

The samples tested in the shear experiments are two mating, initially rough, tension cracks. Each crack is cemented to a 7x7x6 inch steel frame (figure 8). These steel frames are placed in and then fixed to the shear boxes.

Steps in preparing a sample for a shear experiment:

1. Cutting a tension crack down to size with a diamond saw, so it fits into the steel frame.

Samples were cut in a rectangle shape to make area measurement easier. In the direct shear system configuration used, where the lower block moves while the upper block remains fixed in place, the sheared area may change during a test if both samples are of the same size. In order to ensure that the shear area remains constant during the entire test, the upper sample is cut a little shorter than the lower sample. The length difference dictates the maximum shear distance in which the sheared area remains constant. In all samples the difference is at least 20 mm.

2. Placing the cracked samples in the steel frames and cementing them. The cement that fixes the samples to the steel frames is designed to have strength of 30 MPa. The cement is prepared using water to cement ratio of 0.62 and a drying period of 14 days. When cementing the lower sample it was made sure that the entire surface is elevated as little as possible to ensure it is above the cement. To make sure the surfaces are perpendicular to the normal piston, the upper surface was placed on the lower one and adjusted with a leveler. After the lower block is dried the upper surface is placed on it, in a perfect match, and is cemented as well.

3. Calculating the sample area. The measured area is of the smaller upper surface. The area calculation is done to allow the calculation of stresses applied on the samples. Length and width of the samples were measured manually.

3.6 Geometrical measurements of the surface

In order to capture the topography of the fracture surfaces, both before and after they are sheared, they were scanned by a laser profilometer. In this research the ConoScan 2000 laser profilometer manufactured by Optimet, Optical metrology Ltd. was used (figure 16). Our measurements were performed at The Racah Institute of Physics, The Hebrew University of Jerusalem, with the help of Dr. Eran Sharon and Dr. Gil Cohen.

Figure 15: ConoScan 2000, a non contact Laser profilometer.

Specifications

The ConoScan 2000 is a modular, portable 2-D non-contact profilometer -Surface scanner (figure 16).

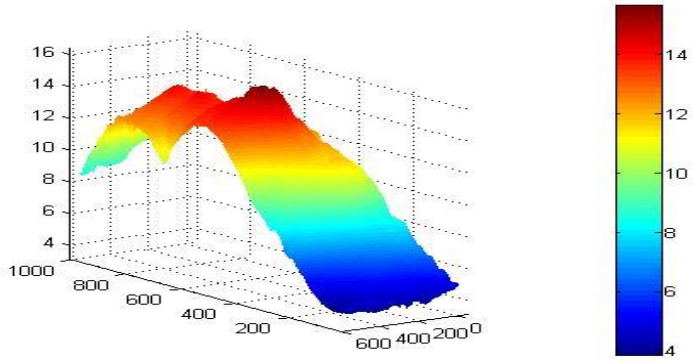

Figure 16: Example for tension crack surface scanned with the ConoScan 2000. Data is displayed using Matlab software, the horizontal axis units are $10^{-4}m$ while the normal axis units are $10^{-3}m$.

A rotational 180° swivel arm enables profile measurements of an object in different directions without moving it from the platform. Interchangeable lenses of the sensor offer down to 0.1 µm precision and working ranges of over 200 mm. The profilometer scans surfaces using 640 parallel laser beams in a single scan and its main advantage comparing to other similar instruments is the scanning speed. The space between the laser beams ranges from 29µm when using the smallest lens to 9µm when using the biggest lens

Planning and performing scans

The ConoScan 2000 is controlled by software installed on a computer connected to the scanner. In order to initiate a scan a few parameters must be entered:

- Start point and total scan length
- The number of measure points to be sampled during the scan.

These parameters dictate the spacing between measure points in the direction of the scan. In this research a spacing of 100μm in the direction of the scan was used in all scans. In order to scan the exact same surface before and after shear a mark was set at the start point of the scan and the end point and was continued to the sides of the sample where it couldn't be destroyed during the shear test.

In the user interface there are: real time display of the data, measurements noise line and brightness control. The measurement noise line should be well below the measured data, if the noise is close to the measured data or above it the brightness must be adjusted until the noise is well below measured data.

After a scan is complete it is saved in a text file. The data size of the surface scanned is always 640 points perpendicular to the shear direction and varies from 700 to 1000 points depending on the length of the sample. This means that every single scan covers an area of about ~ 1500mm^2 including approximately half a million points. Before the surface data is processed filter codes are applied on it. The filter codes delete points that are clearly measurement errors ("spike" points above or below the surface which do not exist on the real surface) and replace them with a best fit average of the surrounding points. It is important to note that filtering affects less than 5% of the points and thus does not affect the statistical characteristics and the roughness analysis.

Chapter 4: **Mechanical characterization of the sampled rock**

In this chapter the starting material properties are determined. The petrography was studied through examining thin sections under petrographic microscope. Both dynamic and static elastic parameters (Young's modulus and Poisson's ratio) were determined using ultra sonic velocity tests and unconfined compression, respectively. The compressive and tensile strength of the rock were determined using unconfined compression and Brazilian tests, respectively.

4.1. Petrography of thin section

The rock samples we used are fine grained limestone from top Judea Group of central Israel, it contains different fossils such as: Gryphea, Gastropod (figure 17), Triserial foraminifer etc.

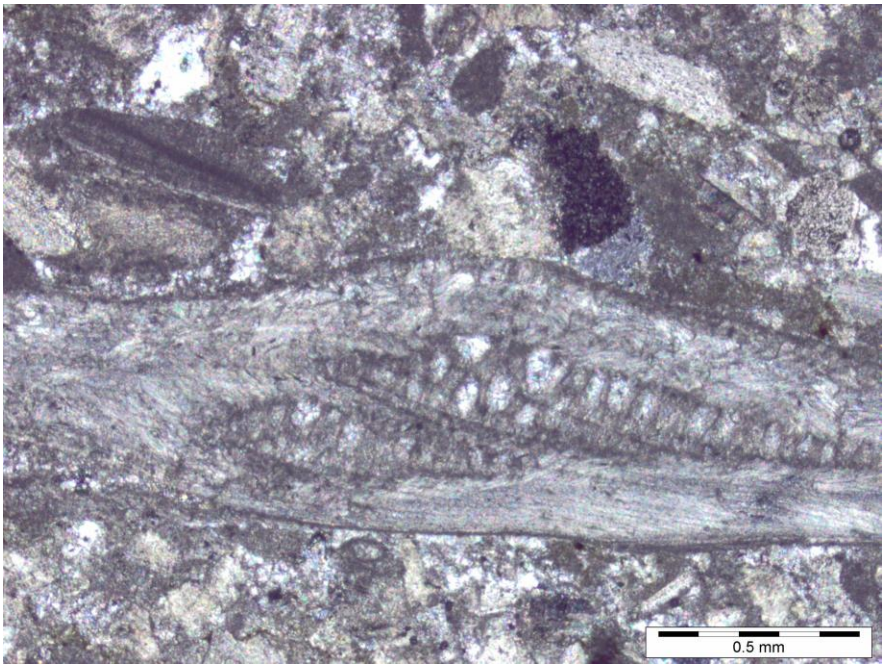

Figure 17: Gryphea valve in echinoderms' bioclasts packestone.

Its average grain size measured from three thin sections is 0.3 mm. The calcite grains have, for the most part, sharp edges and are longer in one dimension than the other. The pores are scarce and are smaller than the grains (under 0.3mm).

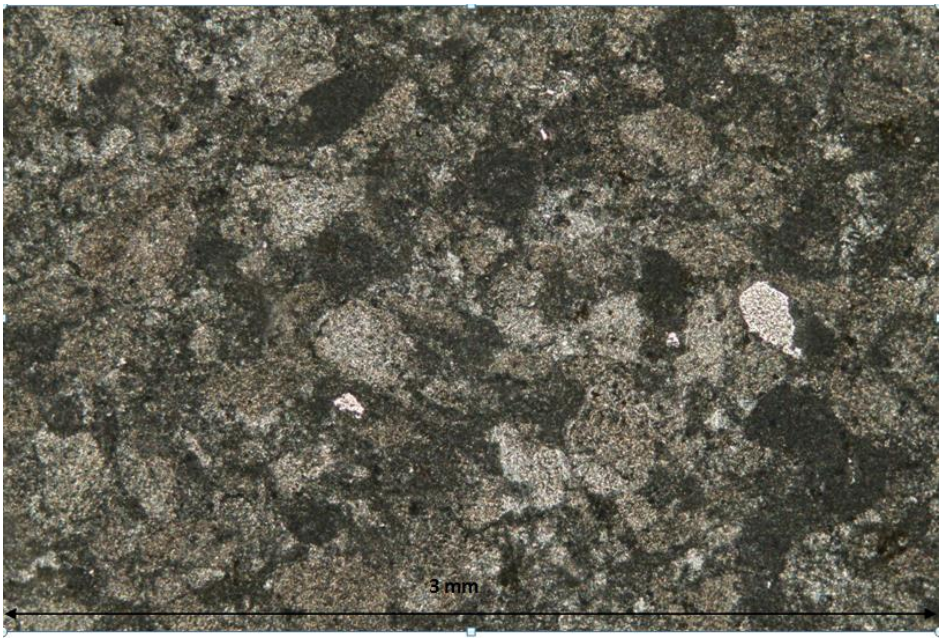

Figure 18: An example of a thin section of the tested limestone.

4. 2 Physical properties

The dry density was calculated by weighing a dry rock sample of known dimensions and simply dividing the mass by the sample volume. The mean density of the samples was 2565 kg/m^3.

For the calculation of the porosity the total sample volume and the known grain density of the limestone (the density of the mineral calcite was used to assume the grain density) were used to determine the volume of the voids. By dividing the volume of the voids by the total volume the porosity was determined. The mean porosity obtained for the samples was n = 5.04%

The dynamic elastic parameters obtained by ultrasonic velocity measurements of solid cylinders were:

$E_d = 69.089\ GPa$,$\nu_d = 0.280$, $G_d = 27.696\ GPa$,

$K_d = 52.454\ GPa$.

Where E= Elastic modulus, ν = Poisson's ratio, G = shear modulus, K = Bulk modulus).

4. 3 Mechanical characterization under uniaxial compression

Uniaxial compression experiments were performed using a Triaxial testing system manufactured by TerraTek, model FX-S-33090 (figure 19- right). The stiff load frame operates using a closed-loop, servo controlled hydraulic system of maximum axial force of 1.4 MN and stiffness of $5x10^9$ N/m. Control can be achieved using either load or displacement monitoring. Unconfined compression tests were run at constant strain rate of $1x10^{-5}$ sec^{-1}.

Several displacement sensors are updating the servo controlled system:

1. Piston displacement is being monitored using a high sensitivity LVDT (Linear Variable Differential Transformer) located outside the vessel near the piston.

2. Load is being measured by a sensitive load cell located in series with the sample stack having a maximum capacity of 1000 KN and linearity of 0.5% full scale.

3. Sample axial (ε_a) and radial strains (ε_{r1}, ε_{r2}) are being recorded using four arm axial and four arm transverse strain cantilever sets (**Error! Reference source not found.**-left), where arm deflection is calibrated to displacement (calibration has been performed prior to the test). The axial cantilever set has a 10% strain range and the radial strain cantilever has a strain range limit of 7%, with 1% linearity full scale for both sets.

The mechanical properties of the limestone samples: the elastic modulus and poison's ratio were calculated using stress-strain relationship measured under uniaxial load and braziliant test.

When fitting a linear line to the axial stress vs. axial strain plot within the linear elastic region, the slope of the line is the value of the elastic modulus (E) (figure 21). The elastic modulus extracted for the rock researched is: $E = 56.983\ GPa$.

When fitting a linear line to the Radial strain vs. axial strain plot within the linear elastic region, the slope of the line is the value of the Poisson's ratio (ν) (figure 22) which for the researched limestone is: $\nu = 0.29$.

Figure 19: Triaxial testing system: 1.4 MN stiff load frame and a 70 MPa confining pressure vessel (right) located at the Rock Mechanics Laboratory of the Negev and the four arm radial and axial strain cantilever gauge system (left).

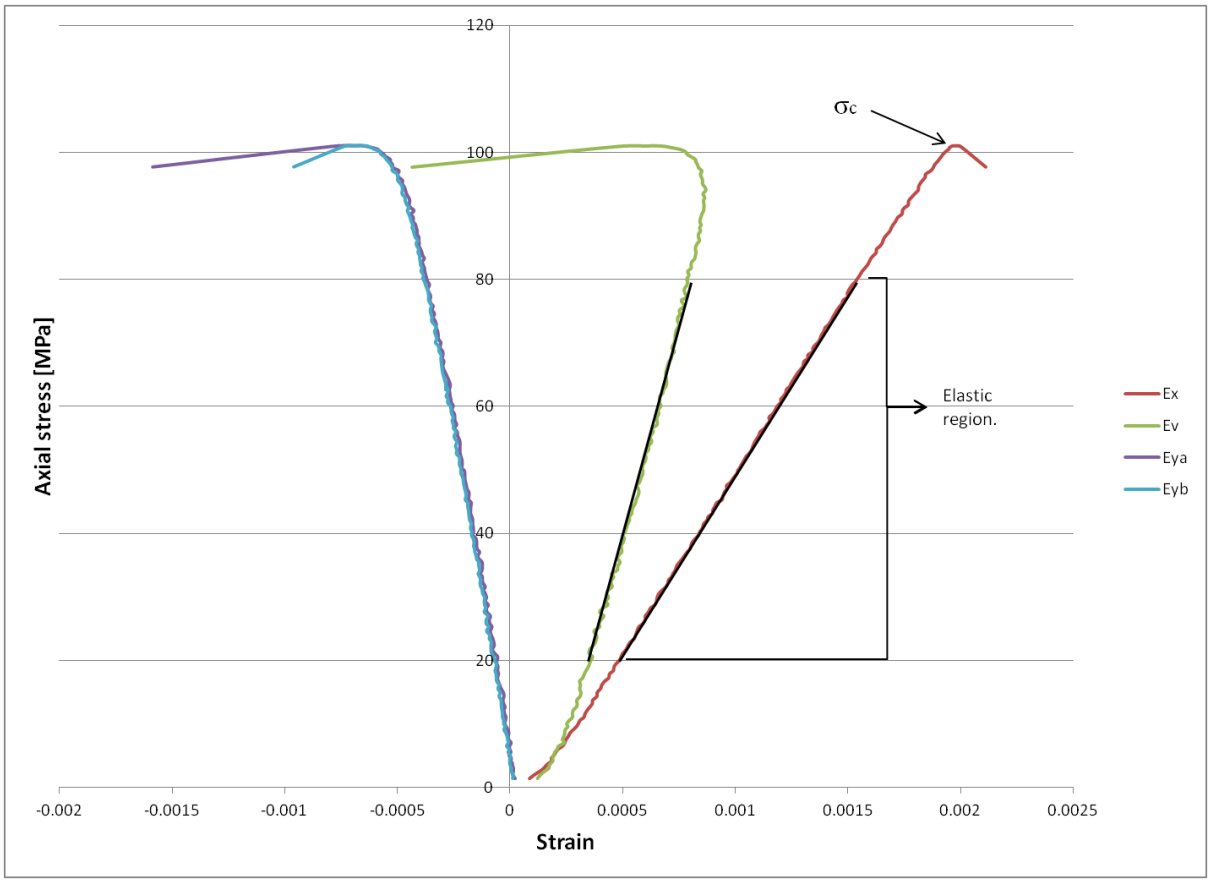

Figure 20: Unconfined compression test. Radial strain is displayed by blue and purple lines, the green line is volumetric strain and the red line is the axial strain. The Black line marks the linear elastic region.

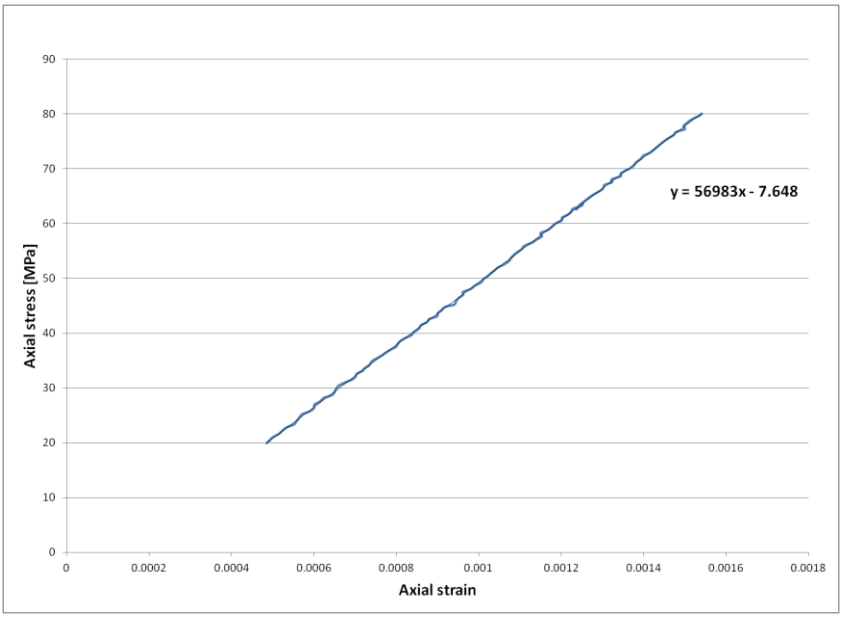

Figure 21: Axial stress as a function of axial strain in the elastic region. The elastic modulus value is determined from the gradient of the best fit linear line .

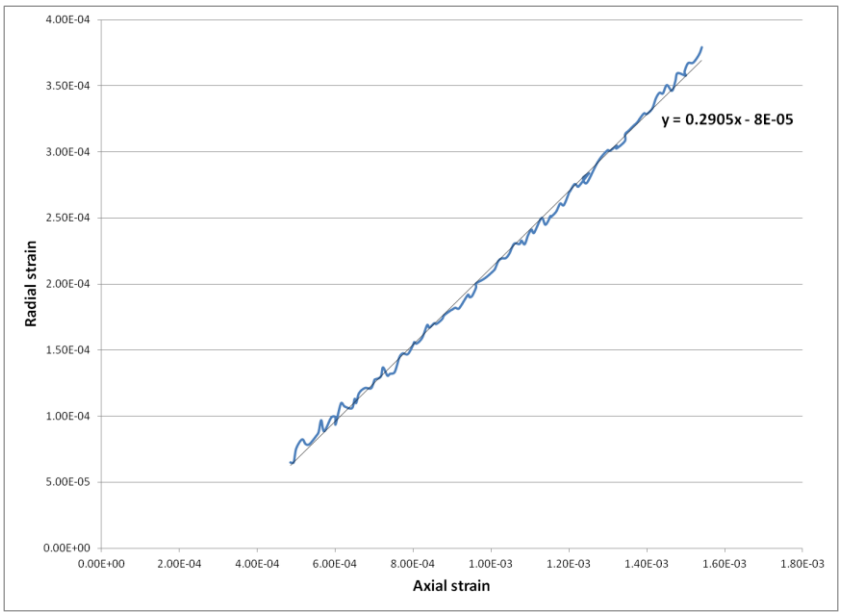

Figure 22: Radial strain as a function of axial strain in the elastic region. The gradient of the best fit linear line is the poisson's ratio.

4.4 The Brazilian test

The Brazilian test measurements were performed using a manual, hydraulic, mini-load frame manufactured by ELE systems Inc. (SBEL model PLT-75) (figure 23). Loading was applied by two diametrically opposed concave loading jaws until failure of the sample was achieved. (Jaeger et al., 2007, Fairhurst 1964)

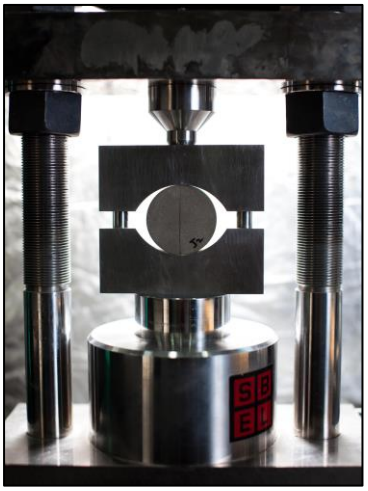

Figure 23: The manual mini–load frame for Brazilian tests- SBEL model PLT-75, with oil shale sample after testing- a typical vertical fracture can be noticed (photo by Yorai Liberman).

Two Brazilian tests were performed in order to determine the tensile strength (σ_t) by indirect tension applied by means of the Brazilian test. The two samples, T1 and T2 were cracked at 13.5KN and 13KN respectively (figure 24) yielding a tensile strength of 5.83MPa and 5.54MPa for samples T1 and T2, respectively.

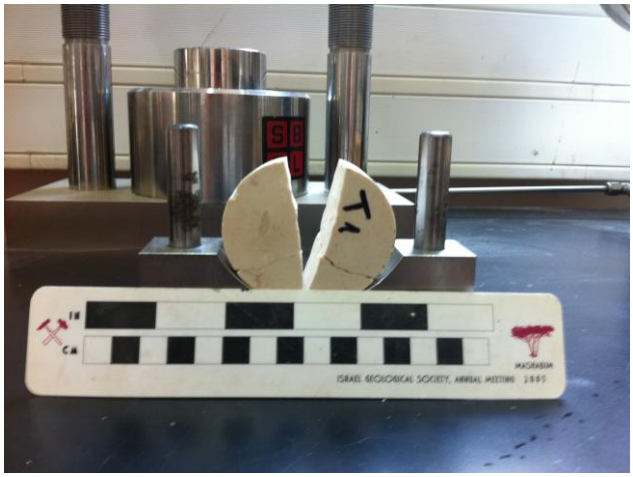

Figure 24: Sample T1 after the Brazilian test.

5. Results

5.1 Shear strength of tested surfaces

In this section direct shear test results are presented (figures 25-29). All the shear tests presented in this paper were performed under a constant normal stress of 2MPa and under an imposed constant shear rate of 0.05 mm/s. The results of each test are plotted as shear stress (blue) and dilation (red) vs. displacement (two y axes). The surfaces to be tested are placed in perfect match at the beginning of each test. The elastic limits of the interface are reached at the first peak in shear stress and the first asperities are sheared. The peak represents the concentration of stresses until the shear strength of the asperity material is reached and the asperity breaks. As the asperity fails and movement is achieved the stresses are released. The shear stress decline is stabilized after a certain amount of displacement and does not fluctuate significantly for the rest of the test - this is the residual shear stress.

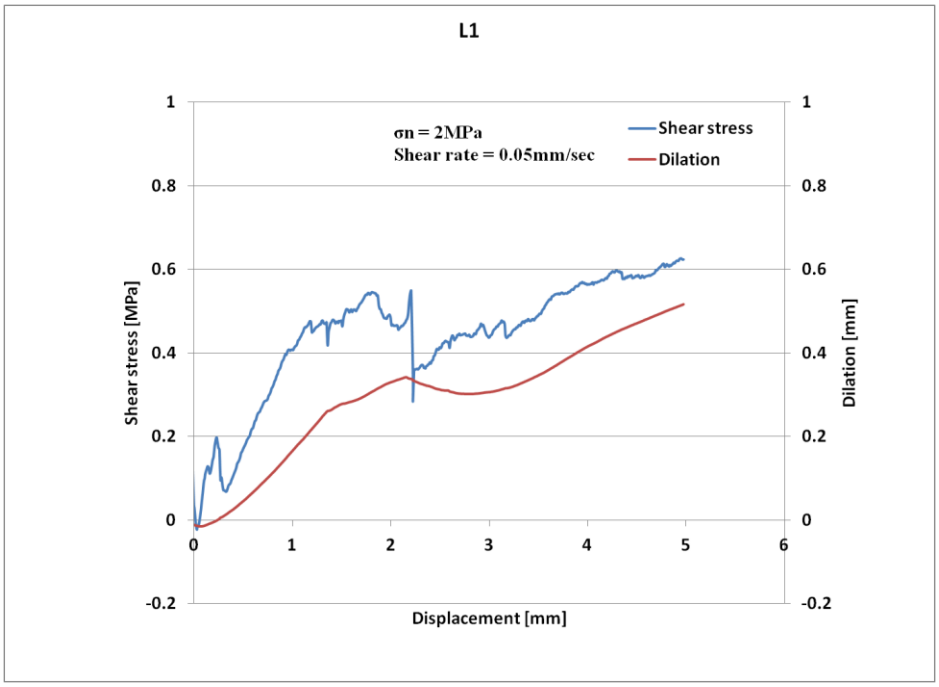

Figure 25: shear stress (blue) and dilation (red) of a tension crack sheared to 5mm using the direct shear system plotted as a function of displacement.

Figure 26: shear stress (blue) and dilation (red) plotted as a function of displacement; the total displacement in this test was 7.5mm.

Guy Davidescko, Evolution of Surface Roughness Through Shear. M. Sc. Thesis. Dept. of Geological & Environmental Science, BGU.

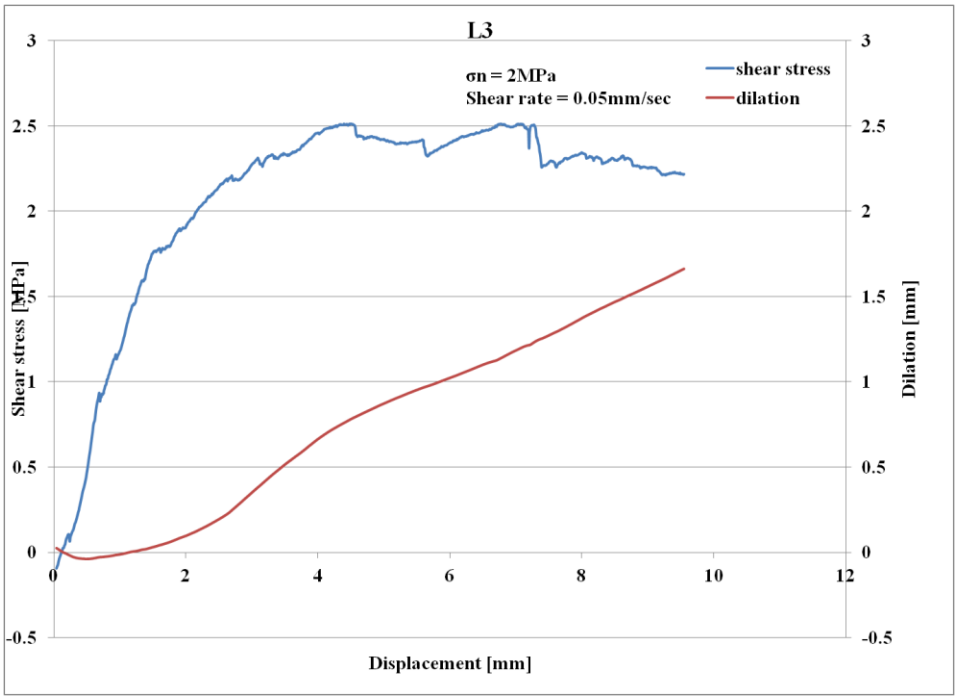

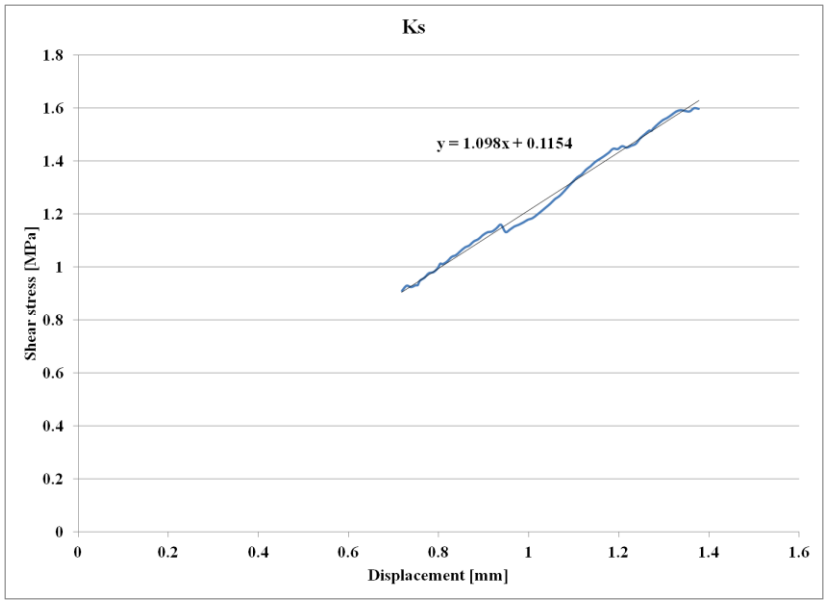

Figure 27: shear stress (blue) and dilation (red) plotted as a function of displacement; the total displacements 10mm (top graph). The bottom graph shows the determination of Ks.

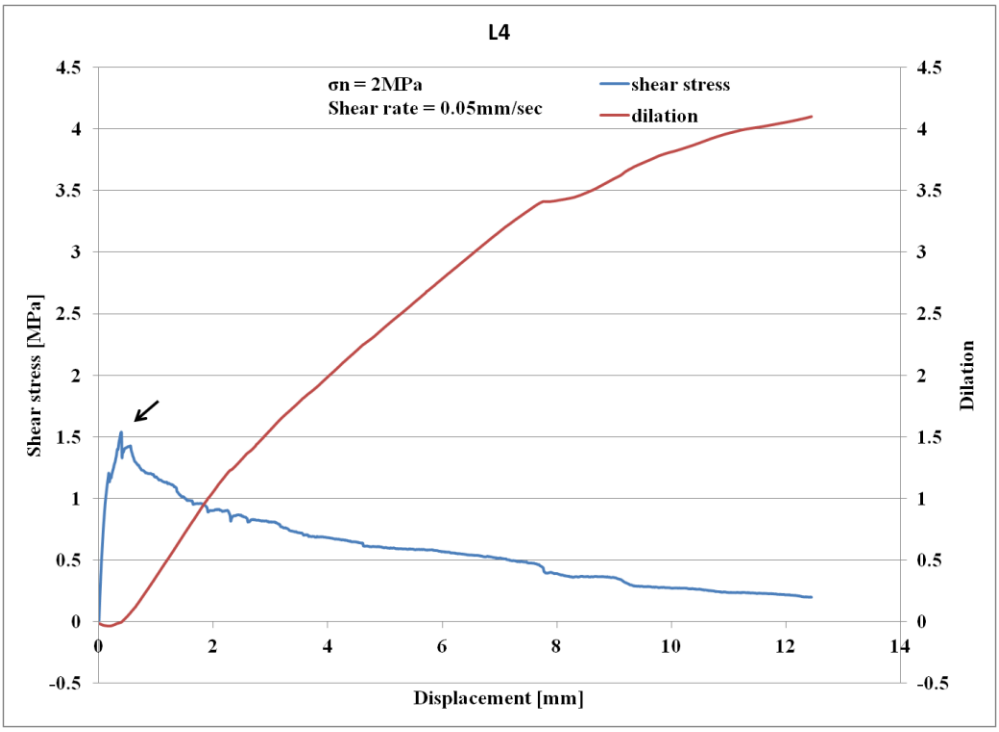

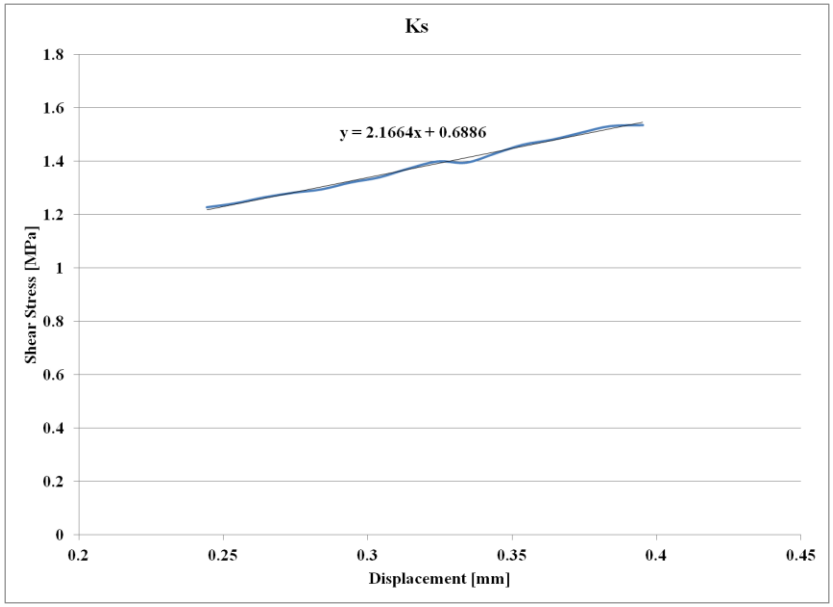

Figure 28: shear stress (blue) and dilation (red) plotted as a function of displacement; the total displacements 12.5mm (top graph). The bottom graph shows the determination of Ks.

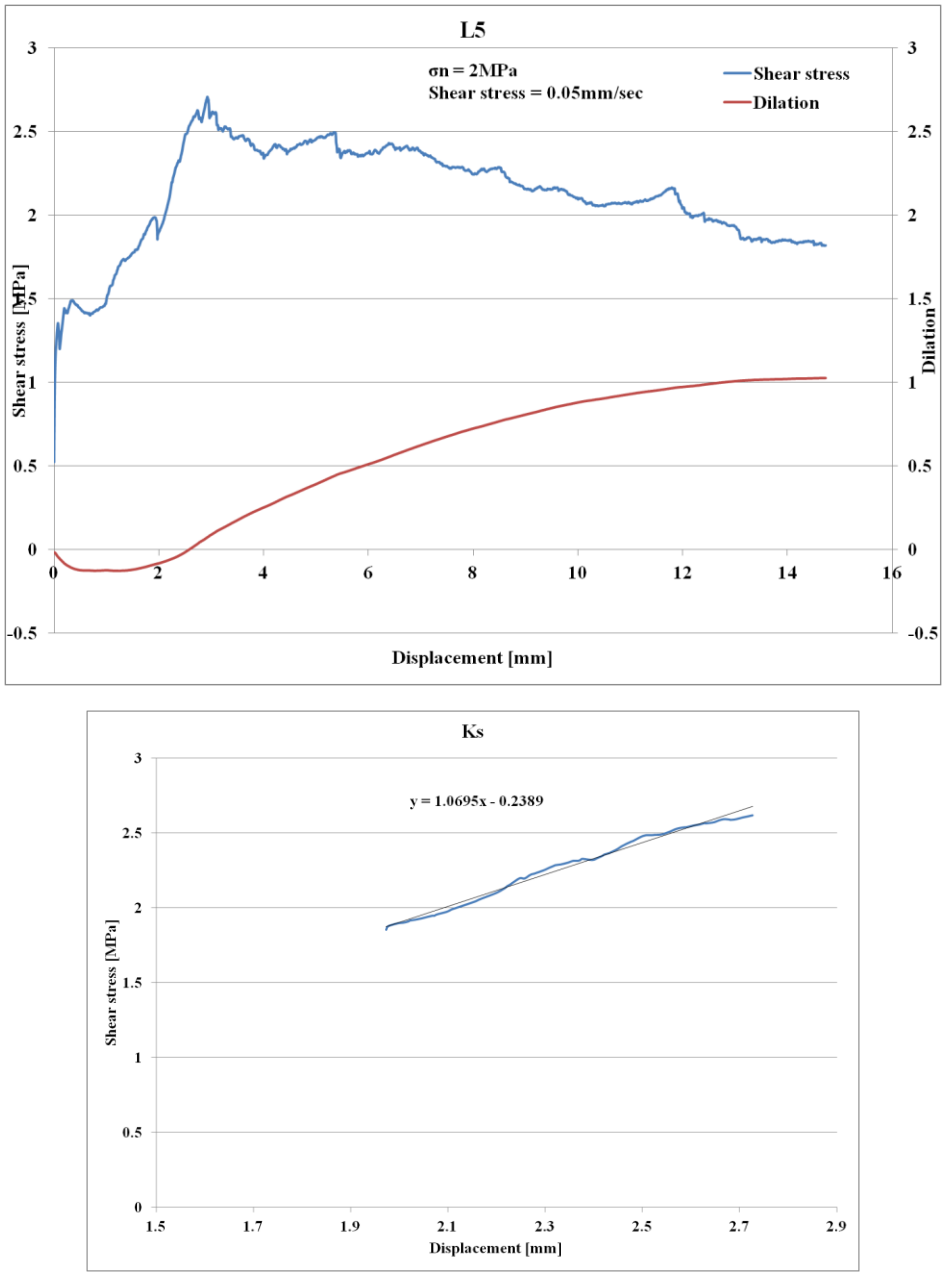

Figure 29: shear stress (blue) and dilation (red) plotted as a function of displacement; the total displacements 15mm (top graph). The bottom graph shows the determination of Ks.

Three tension cracks displayed in their shear tests a peak behavior in shear strength (τ_p) followed by residual shear strength (τ_r). These were the three tests sheared to 10mm, 12.5mm and 15mm:

τ_p: 2.50Mpa, 1.56MPa and 2.71MPa respectively and an average of 2.25MPa.

τ_r: 2.25MPa, 1.35Mpa and 1.65MPa respectively and an average of 1.75MPa.

The linear slope of shear stress vs. shear displacement determines the Shear stiffness (k_s). The k_s values of the tension cracks sheared to 10, 12.5 and 15mm are: 1.09$\frac{MPa}{mm}$, 2.11 $\frac{MPa}{mm}$ and 1.06$\frac{MPa}{mm}$.

The first two tests have shown local peaks in shear stress but no residual shear stress was reached - the shear stress continued to grow after each local peak. This behavior is likely to be the result of the roughness profile geometry.

The shear tests display a lot of fluctuations in the shear stresses - these fluctuations are probably due to the irregularity of the tested surfaces. The shear stresses reached in the first two shear tests are low, indicating that the resistance met in these tests was lower than the following three tests. It is likely that if the displacement continued the same shear stresses would have been reached.

5.2 Roughness evolution.

The main aim of this research was to quantify the roughness evolution of the rock samples as a function of slip distance. Here we present results of five experiments made under normal stresses of 2MPa with slip amount from 5mm to 15mm. The evolution of the surfaces is analyzed statistically and presented based on the dense geometrical measurements in Figs. 33-37.

5.2.1 Data processing

We used two different analysis types to calculate the roughness of the sample parallel to the slip direction (Brodsky et al., 2011). The first analysis method implements a numerical RMS code, which calculates the RMS values for any given profile length along the surface and averages the values. As the database is extremely large, a reliable average of RMS values of any given length scale along the surface can be plotted (Figure 31). The second analysis method uses the PSD values to characterize the scale dependence roughness (Power et al., 1988). In the present analysis we use the code of Sagy and Brodsky (2009), which is based on Press et al.,

(2007), section 13.4.17 that averages the values of all 640 profiles to one RMS function of length scale.

Figure 30 displays an example of a single profile of a virgin tension crack without shearing, measured with the profilometer whereas figure 31 is the average of the RMS values of 640 such profiles.

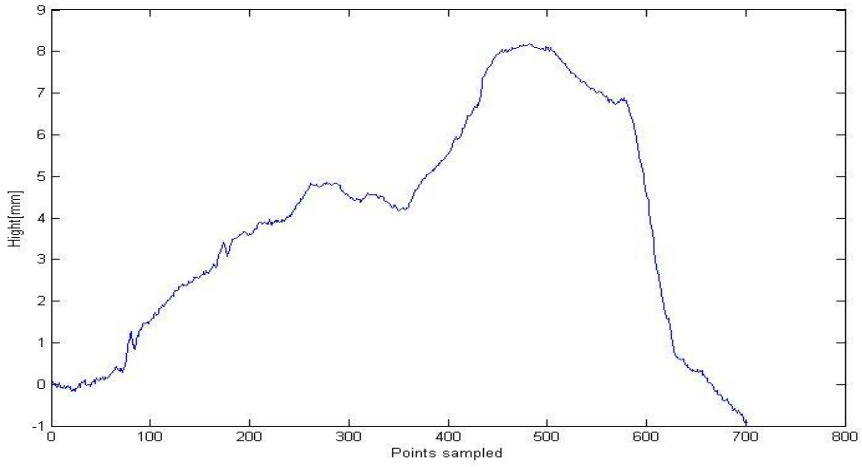

Figure 30: A single scanned profile, the distance between each sampled point is 100 μm making this profile total length 7 cm.

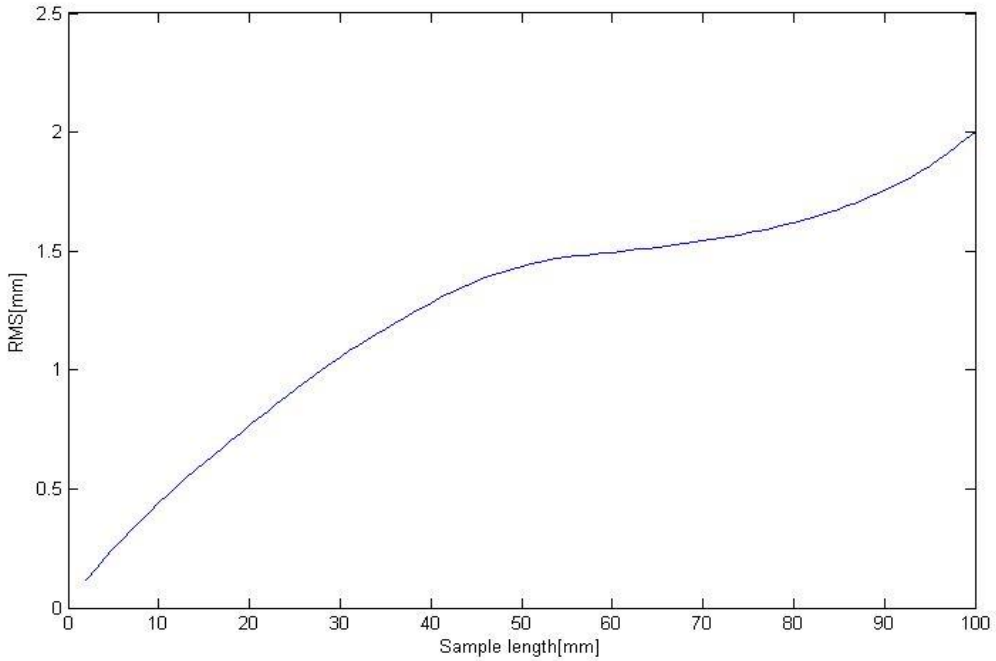

.

Figure 31: RMS roughness as a function of profile length, the RMS roughness is the result of the average of 640 profiles.

5.2.2 Roughness variation with profile length and slip distance

The evolution of the roughness can be measured using different methods (Wang and Scholz 1994, Power et all 1988, Chen et al 1993). In this section the evolution is first presented by subtracting the surface roughness after the test from the surface roughness before the test (figure 32). Using this mode of presentation, the affected zones on the surfaces and the connected amplitudes can be visualized. An example is presented in Fig. 32 which displays the topography changes in two different surfaces that have been subjected to shear: the first surface sheared to 7.5 mm and the second sheared to 15 mm. The surface that was sheared to a longer distance displayes larger variations in amplitude differences. These observations demonstrate that roughness evolves during shear. Moreover, it is clear that there are some zones in both surfaces which have larger amplitude differences than the rest of surface.

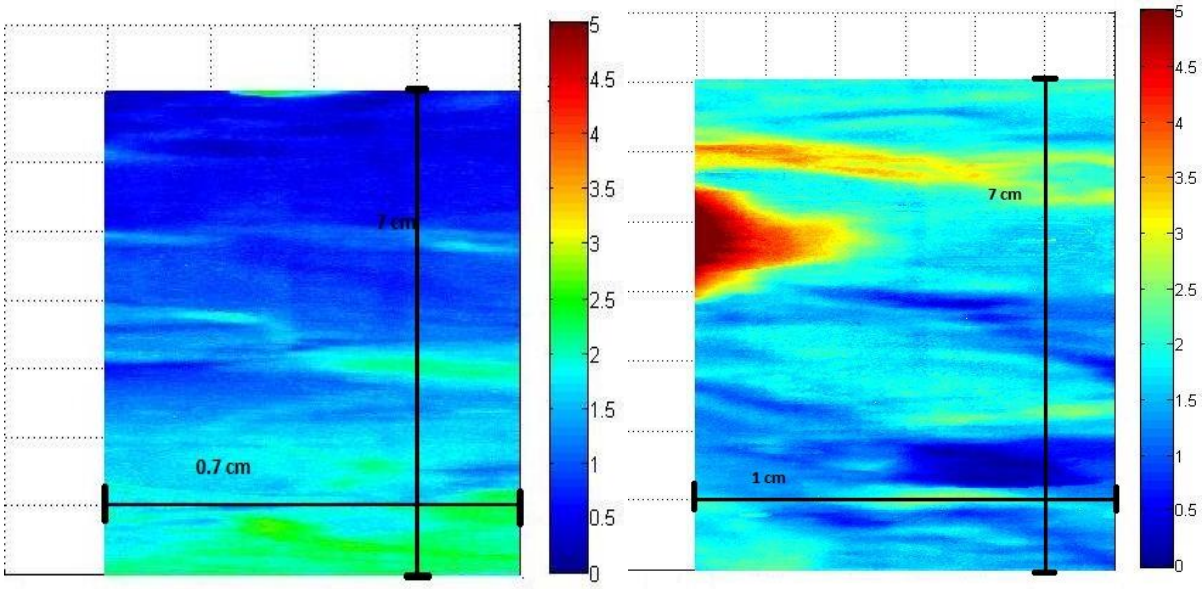

Figure 32: The difference in asperity heights after 7.5mm shear (left figure) and 15mm (right figure), the color code's units are mm.

A quantitative approach for measuring the roughness evolution of the surfaces as a function of shear distance is by using statistical methods. The roughness characterization is presented in Figs. 33-37, for shear distances of 5 to 15mm using the two methods discussed in Sec. 3.5, (e.g. PSD and RMS). The values were calculated parallel to slip distance for each surface before and after shear. Thus the relative effect of the shear distance can be detected although the initial roughness in the experiments is not identical. The results are plotted by two graphs for each test, one of PSD values and the other of RMS values. In the following figures (33-37) RMS roughness values are presented against profile length and the PSD values are presented against the wavelength.

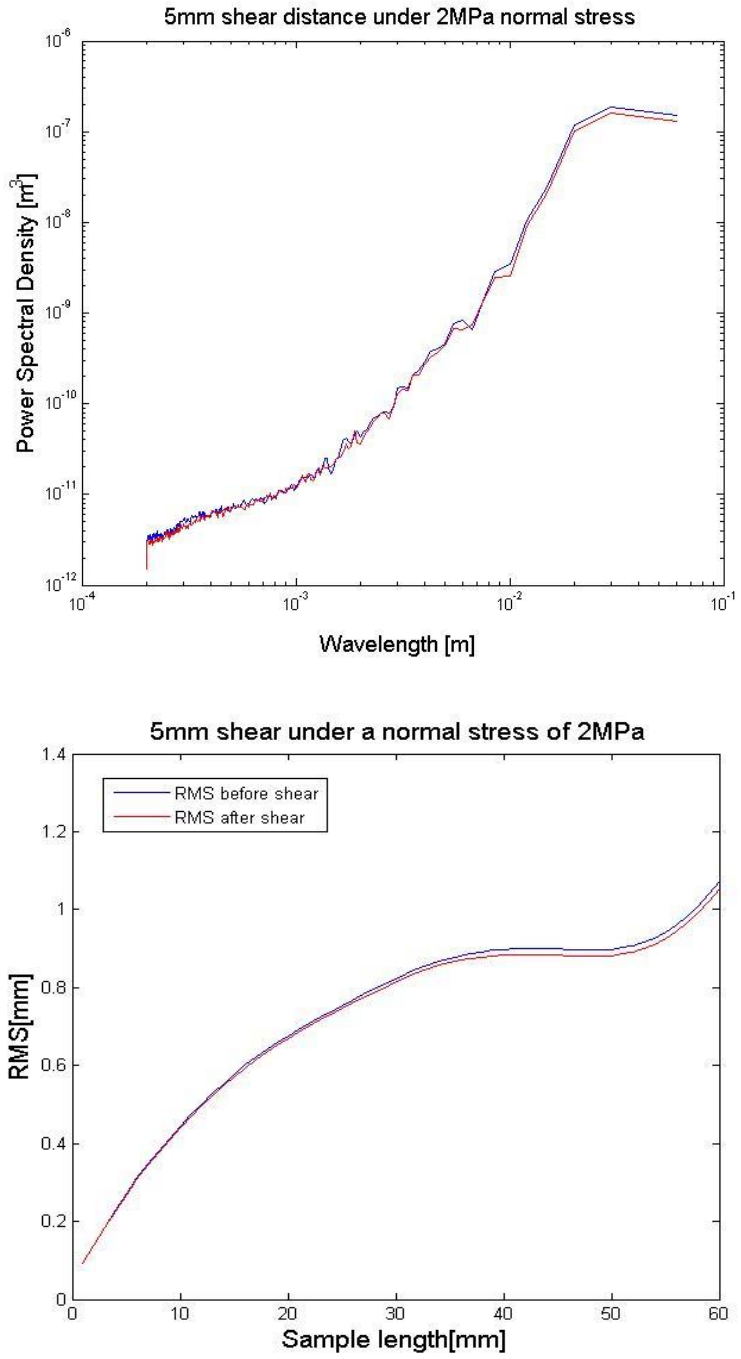

Figure 33: Power spectral density parallel to shear direction calculated from a tension crack sheared to 5mm scanned with a laser profilometer, each profile includes 640 parallel profiles (upper figure) and RMS roughness parallel to shear direction calculated from the surface (lower figure). Both graphs include the values before shear (blue) and after shear (red).

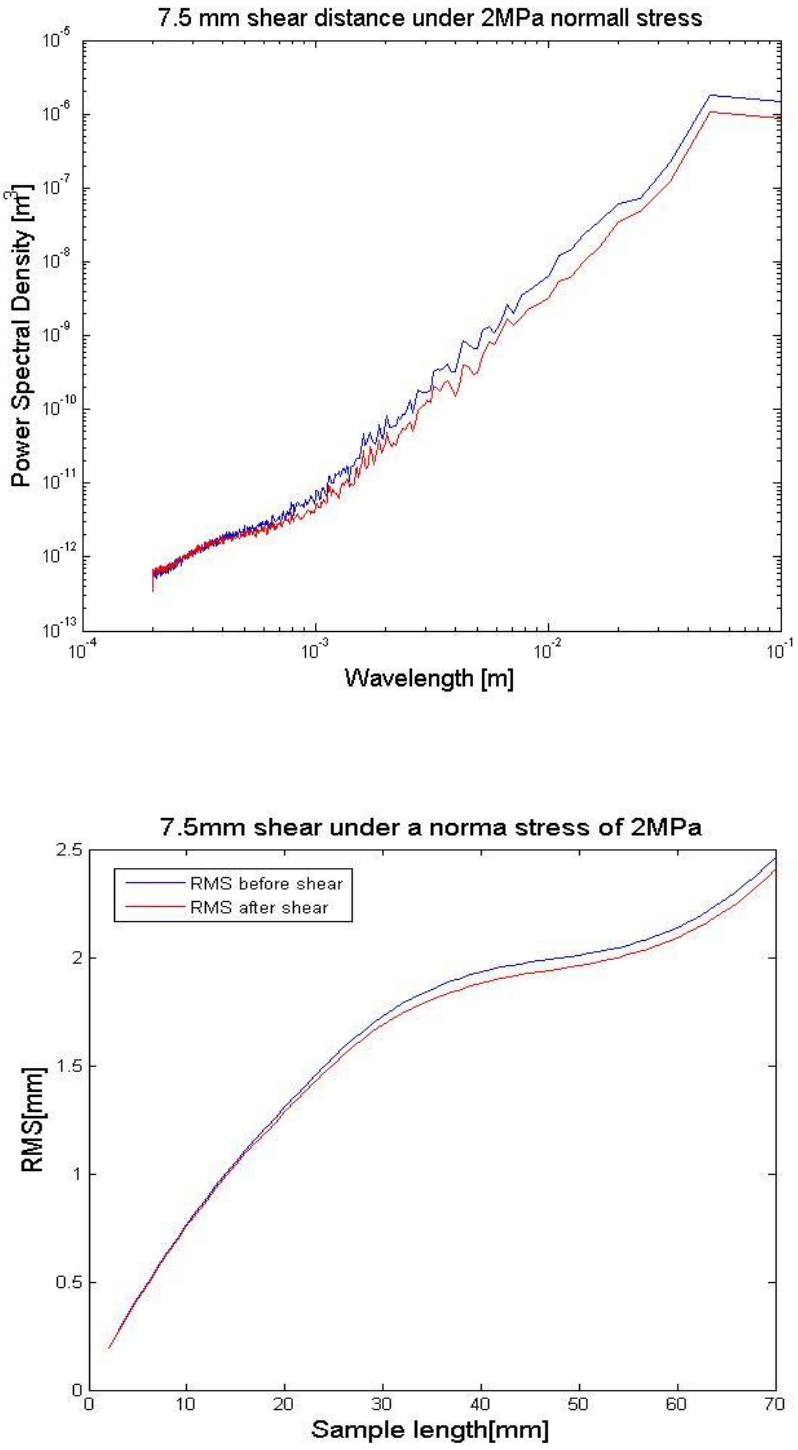

Figure 34: PSD and RMS values as function of measured sample length before (blue) and after (red) shear of 7.5 mm

Guy Davidescko, Evolution of Surface Roughness Through Shear. M. Sc. Thesis. Dept. of Geological & Environmental Science, BGU.

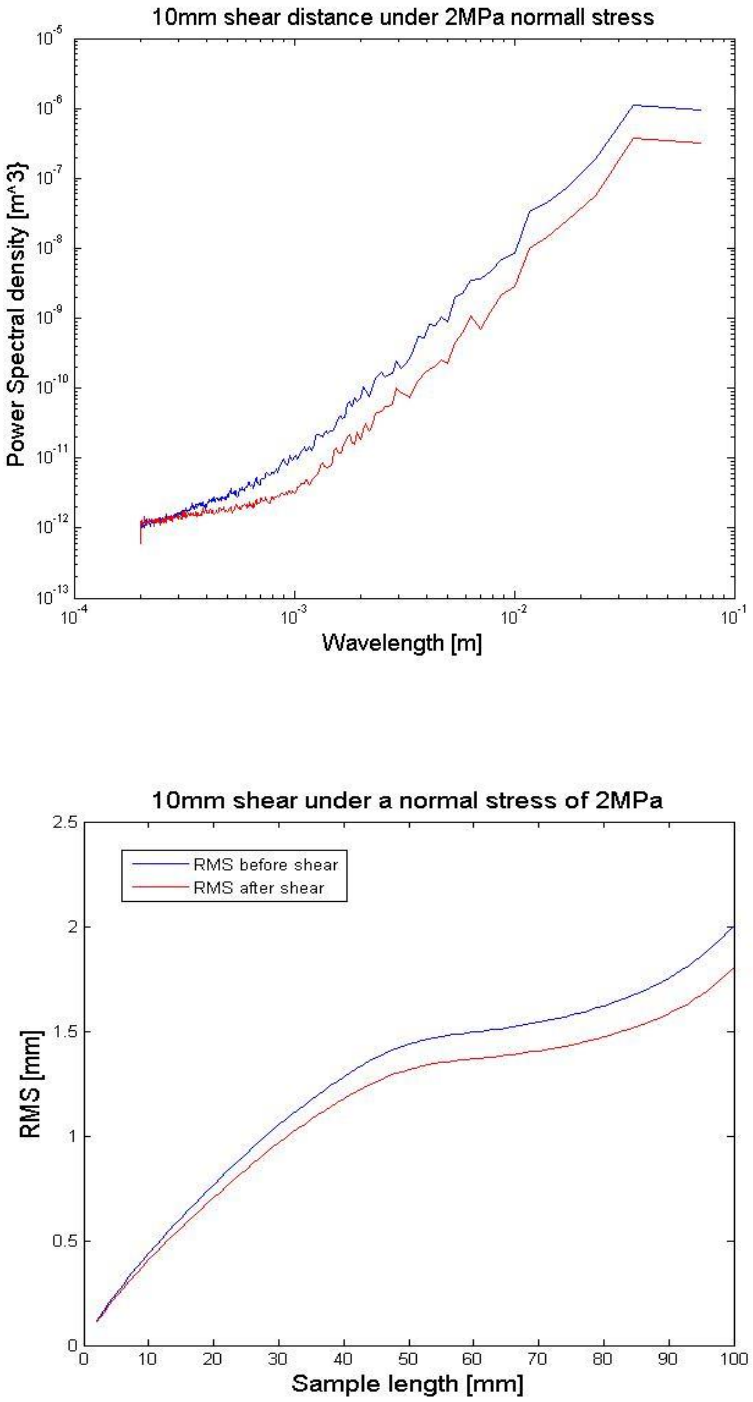

Figure 35: PSD PSD and RMS values as function of measured sample length before (blue) and after (red) shear of 10 mm

Guy Davidescko, Evolution of Surface Roughness Through Shear. M. Sc. Thesis. Dept. of Geological & Environmental Science, BGU.

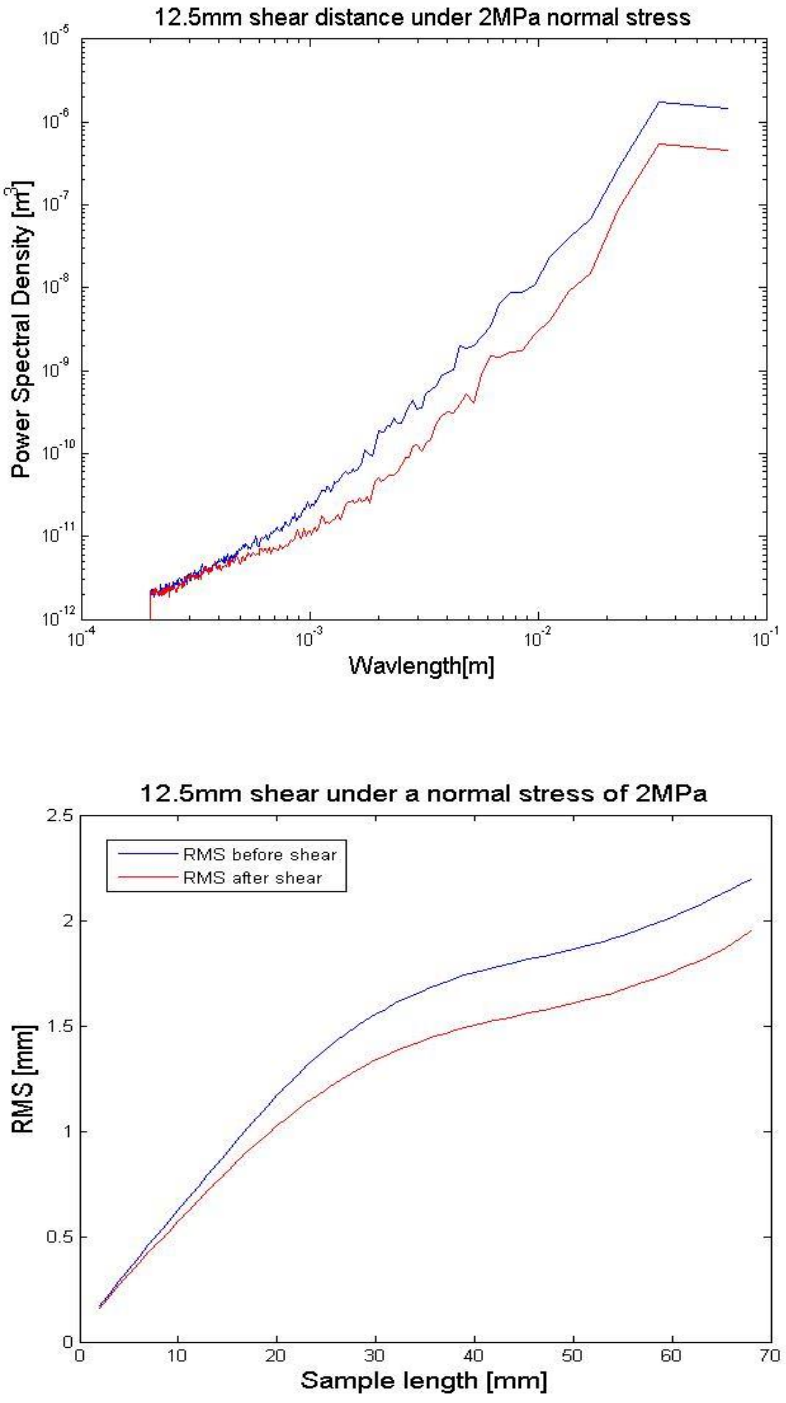

Figure 36: PSD and RMS values as function of measured sample length before (blue) and after (red) shear of 12.5 mm

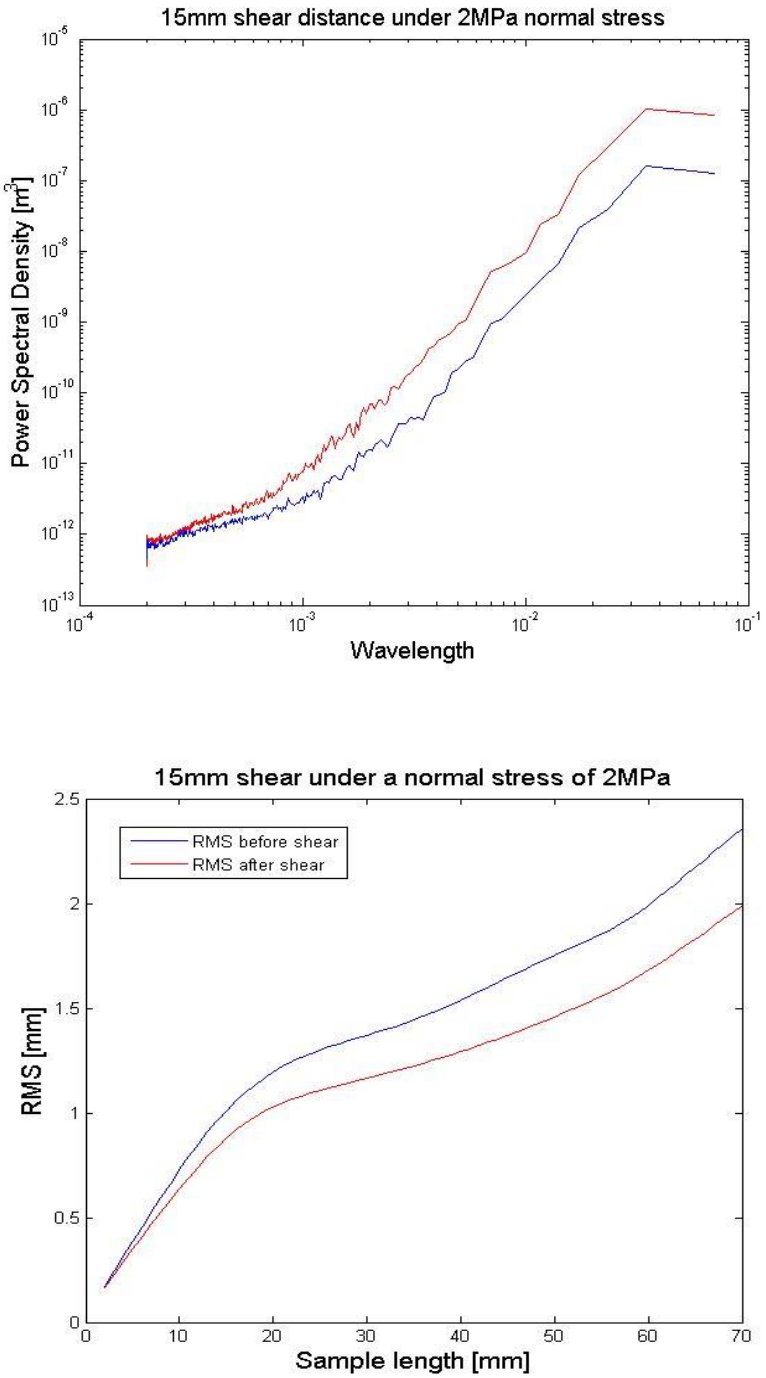

Figure 37: PSD and RMS values as function of measured sample length before (blue) and after (red) shear of 15 mm

Guy Davidescko, Evolution of Surface Roughness Through Shear. M. Sc. Thesis. Dept. of Geological & Environmental Science, BGU.

The laboratory experiments performed quantify the geometrical evolution of rough slip surfaces in hard limestone. Figure 33 shows that for 5mm of shear the roughness is almost unchanged and geometrical variations are mostly below the measurement resolution. However, we will show later (Fig. 37) that even under this small amount of displacement roughness degregades. When observing the RMS roughness and PSD before and after being sheared to 7.5mm, a visible difference appears between them (Fig. 34). The values of the RMS roughness and the PSD after shear are lower than before shear along all measured scales. An important observation which is clearly portrayed in Figures 34 – 37 is that large scales are affected by shear displacement more than small scales. For example, Fig. 34 demonstrates that the RMS difference at a scale of 10 mm is $5 * 10^{-3}$mm, while at a scale of 50mm it is 0.04mm. This trend continues as the displacement distances grow to 10, 12.5 and 15 mm. In the two samples sheared to 12.5 and 15mm a difference in the RMS roughness and PSD is easily visible even at the smallest scales. Fig. 38 shows the RMS differences in all the experiments.

The results demonstrate that roughness decreases under shear and the surface is polished as a function of slip distance. The amount and nature of roughness degradation as a function of measuring scale is not trivial. In summary, the results presented in Figs 34-38 demonstrate that:

1. Shearing decreases the RMS and PSD values resulting in roughness degradation at all measured scales.
2. For any given sample, the longer the length scale the greater the difference in roughness (Fig. 38).
3. Differences between initial RMS and PSD to final values increase as the displacement increases at all measured scales.

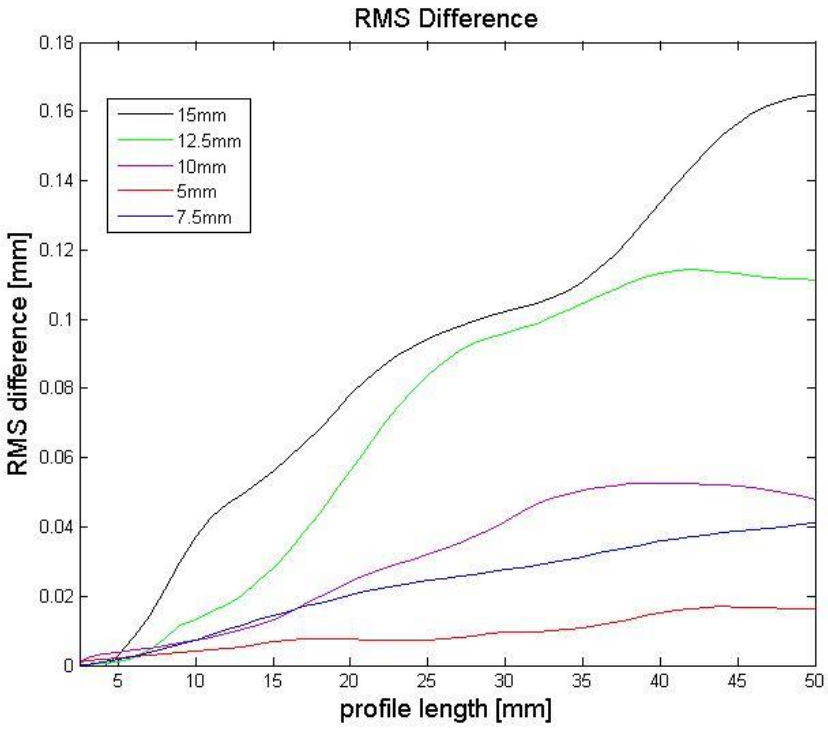

Figure 38: RMS roughness differences. Each line represents the RMS roughness before being sheared subtracted by the RMS roughness after being sheared.

Chapter 6: Discussion

In this chapter we discuss roughness evolution of slip surface as a function of slip distance, under the conditions of our experiments as well as the applications to natural faults. First we explain how initial surface geometry influences stress and slip history during the experiments. We then analyze the roughness evolution dependence on spatial scales and slip amount by normalizing the experiments and comparing between them. Finally, we discuss the relevance of our results to the evolution of natural slip surfaces by comparing them to field measurements and to former laboratory experiments.

6.1 Geometrical influence on stress and slip history during the experiments

The two surfaces were placed on top of the other at a perfectly matching position before the tests began. With onset of shear stress sliding developed until peak shear stress was attained, indicated for example by the arrow in Figure 28. Beyond peak stress the asperity material begins to fail and consequently the shear stress decreased (Barton 1973, 1976). As the relative motion continued, more asperities interacted with each other and more stress fluctuations were observed (Figs. 25-29). The fact that in all our experiments the sample continued to dilate under shear, even after reaching residual stress (Figs. 25-29), indicates that at least some of the asperities "ride" over other asperities in the opposite surface (Patton 1966).

Moreover, our roughness measurements demonstrated that under the conditions of slip distances and normal stresses that were applied in the present series of experiments, the tested surfaces have been smoothed gradually as roughness degraded. This scenario can be explained by assuming that slip of the asperities is partly absorbed by yielding of asperities and partly by riding on the asperities one on top of the other (Scholz., 2002) beyond peak stress but before steady state sliding is reached. We believe that the fluctuations in shear stress are governed by the evolving surface geometry during slip.

6.2 Roughness evolution as a function of spatial scale and slip amount

One of the main observations in our experiments is that at relatively large scales, the PSD as a function of the wavelength (λ) decreases by a constant ratio. Here we explain the mechanical source for the differences between the roughness before and after slip. Fig. 39 shows an example of one surface profile (blue) when every geometrical fluctuation is divided by a constant (red). Such polishing is expected to be a product of shear deformation of matching surfaces when all scales are affected and yield by shear by the same amount.

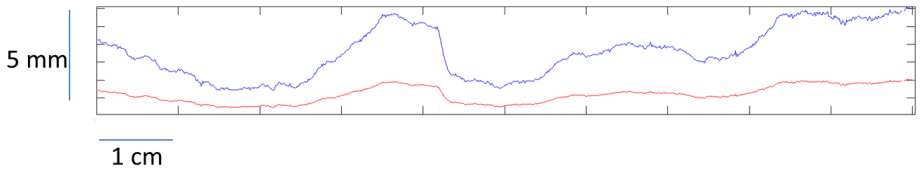

Figure 39: A single profile of a rough surface (blue) when every geometrical fluctuation is divided by a constant (red)

However, as we already noted (Sec. 6.1), our experiments indicate that such roughness degradation, or surface polishing, only occurs at relatively large scales. The parallel linear PSD slopes that have been observed in our experiments (Figs. 33-37) at these scales suggest that the roughness might be defined by a power law and that the only difference in roughness at these scales is the coefficient of the power. On the other hand, at small scales the PSD curve of the samples after slip is more moderate, suggesting that small scale geometrical fluctuations are less affected by the polishing.

The mechanism that might explain the roughness evolution in our experiments is that as displacement begins, shear stress concentrates at the contact points between the interfaces. Displacement can commence only when the interlocking asperities that prevent the interface from sliding fail when stress concentrations exceed the shear strength of the asperity material. However, not all the asperities are completely smoothed by the end of the shearing cycle, as evident by the dilation the surfaces exhibit during post peak shear displacement (Sec. 5.1). We argue that when displacement progresses the relatively larger asperities are more likely, statistically, to interact with one another (Power et al., 1988) and consequently to be smoothed to a certain amount. The smaller asperities, however, are less likely to be

affected so long as the total amount of shear displacement doesn't exceed the tested displacement range in this study, namely 5 – 15 mm. When relatively large asperities interlock they yield but are not totally decapitated. Therefore slip involves riding up on asperities, as evident by the dilation (Figs. 25-29), as well as shearing through them. As shear displacement that involves failure of the asperity material as well as dilation continues, new space can be generated between the surfaces and consequently the actual contact points between the originally mating surfaces will decrease. Furthermore, asperities of smaller height amplitude are less likely to interact with asperities on the opposite surface.

We now examine how the slip amount affects roughness by comparing entire sets of our experiments. Although the roughness profiles of all the tested tension cracks were similar, they were not identical. In order to further characterize the roughness evolution and fully compare the roughness results from the different shear tests we normalized the PSD and RMS results by dividing the results after being sheared by those before being sheared (Figs. 40 and 41).

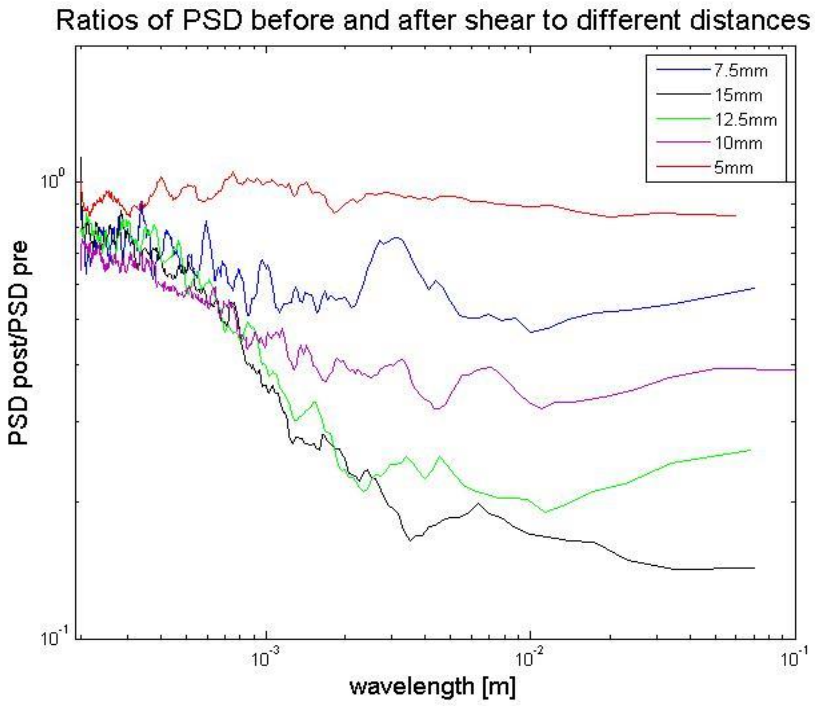

Figure 40: PSD ratios. Each line represents the ratio of the PSD after being sheared to the PSD before being sheared for a certain shear distance. The distances are detailed in the key.

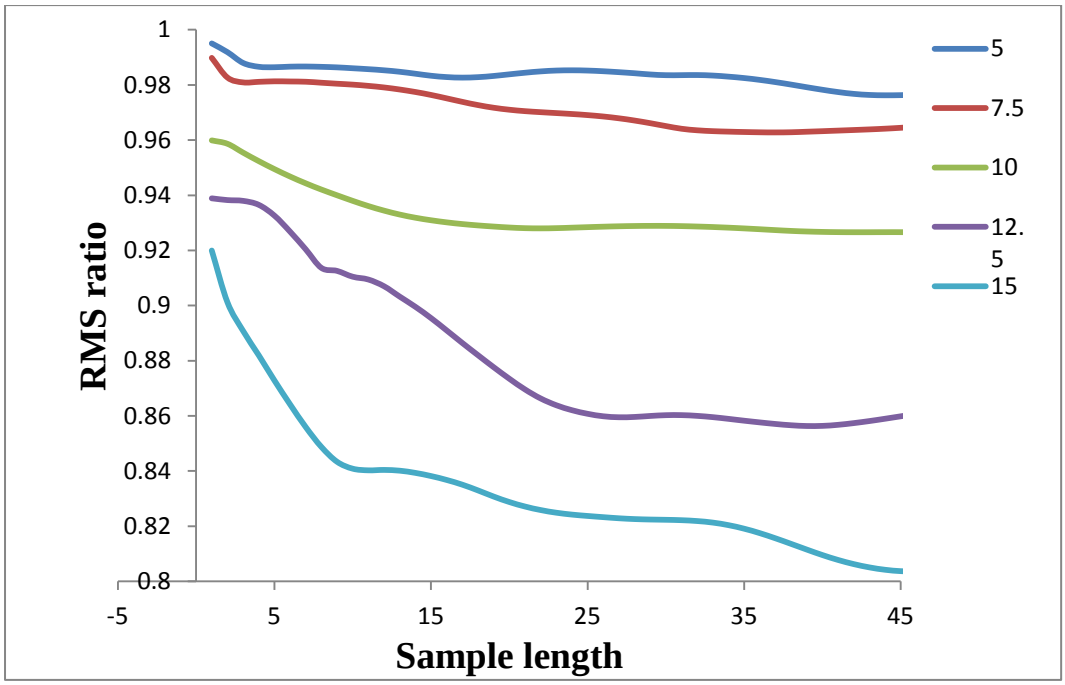

Figure 41: RMS ratios. Each line represents the ratio of the RMS after being sheared to the RMS before being sheared for a certain shear distance. The distances are detailed in the key.

Figures 40 and 41 display a decrease in the PSD and RMS ratios respectively to a certain length scale where the ratios stabilize. The ratios decrease to a lower value as displacement increases and the length scale at which the ratios stabilize increases. According to this picture, the roughness of a fault that has undergone some slip can be described by two slopes (in a PSD plot). The roughness slope which describes the small scales has a lower power than the initial roughness. This slope breaks off at a certain scale and the power increases. The power of the second slope is parallel to that of the initial roughness. At relatively large scales, the PSD as a function of the wavelength (λ) decreases from $K_1 * f(\lambda)$ to $K_2 * f(\lambda)$ for any given sample when K_1 and K_2 are constants and $K_1 > K_2$. In summary, the important observations from Figs. 40 and 41 are:

- PSD and RMS values are high at relatively large scales and low at relatively small scales in each test.
- The maximum polishing (the lowest ratio of pre-shear to after shear) increases with slip distance.

6.3 Conclusions and implication for natural faults

Direct observations from our experiments demonstrate that surface roughness is evolved during slip in all measured scales in a way that the roughness degrades with increasing shear distances. Specifically, we have shown that:

1. Shearing decreases the RMS and PSD values resulting in surface polishing along all measured scales.
2. For any given sample, the bigger the length scale the greater the difference in roughness (Fig. 38), namely the greater roughness degradation.
3. Differences between initial RMS and PSD to final values increase as the displacement increases at all visible scales.

Therefore, we suggest that polishing during shear sliding generally decreases the roughness function by a constant characteristic value. For example, if surface roughness (RMS) can be defined by a power law such as $H_{1(L)} = K_1 * L^{\beta}$, (Bouchold et al., 1990, Renard et al., 2006, Candela et al., 2012), the RMS as function of the length scale after shear will evolve to $H_{2(L)} = K_2 * L^{\beta}$

When $K_1 > K_2$, H_1 is the RMS before the surface is sheared and H_2 is the RMS after shear.

Our interpretation is that the asperities are fractured and yield during shear, although never by total decapitation. Thus these scales are affected proportionately to their size (Fig. 39). This picture is different than demonstrated by Power 1988 (see Fig. 1) for the roughness of ground sample that was prepared by saw and had decapitated down in a uniform fashion.

On the other hand, we also observed that under the conditions applied in our experiments, small scale polishing is less effective, probably due to dilation during shear. Roughness controlled dilation may decrease under high normal stresses in natural faults (Patton 1966, Byerlee, 1978).

Although we cannot test the hypothesis of self-affinity because in our measurements we were able to sample only three orders of length magnitude, we did not find evidence for general PSD slope moderation as has been suggested by measurements of fault surfaces in the field (Renard et al., 2006, Candela et al., 2012). On the contrary, although roughness

systematically decreases in our experiments, the PSD slope is relatively fixed for relatively large scales. We think that the roughness exponent moderation, which was reported in these works, may be connected to gouge layers that were attached to the surfaces of natural faults during slip and affect the roughness. Sagy et al., (2007), for example, showed that roughness exponents of small-slip faults are relatively high compared to mature faults at small length scales. However, at bigger length scales the roughness exponent is similar and the decrease in roughness can be described only by the decrease in the exponent coefficient.

Patton (1966) has previously observed that friction under low normal stresses is strongly dependant on surface roughness. A decrease in roughness of each scale proportionate to its size will have strong affects on resistance to shear and fault gouge generation of natural faults.

Reference list

Archard, J. F. (1953). "Contact and Rubbing of Flat Surfaces." Journal of Applied Physics **24**(8): 981-988.

Barton, N. (1973). "Review of A New Shear-Strength Criterion for Rocj Joints." Engineering Geology **7**: 287-332

Barton, N. (1976). "The Shear Strength of Rock and Rock Joints." International Journal of Rock Mechanics and Mining Sciences & Geomechanics Abstracts **13**(9): 255-279.

Bouchaud, E., G. Lapasset & J. Planès (1990).” Fractal dimension of fractured surfaces: a universal value ?” Europhysics Letters **13**: 73-79.

Byerlee, J. (1978). "Friction of Rocks." Pure and Applied Geophysics **116**(4-5): 615-626.

Brodsky, E. E., J. J. Gilchrist., A. Sagy. & C. Colletini (2011). "High resolution 3D laser scanner measurements of strike-slip fault quantify its morphological anisotropy at all scales." Geophysics Research Letters **33**(L04305): 10.1029/2005GL025038.

Candela, T., F. Renard., Y. Klinger., K. Mair., J. Schmittbuhl. & E. E. Brodsky (2012). “Roughness of fault surfaces over nine decades of length scales.” Journal of Geophysical Research: Solid Earth **177**(B8): 86-102.

Carpinteri A., B. Chiaia, and S. Invernizzi (2000).” Comments on: Direct fractal measurement of fracture surfaces" Int. J. Solids. Struct **37**: 4623-4625.

Chen, G. & H. Spetzler, (1993). "Topographic Characteristics of Laboratory Induced Shear Fractures." PAGEOPH **140**(1): 123-135.

Dieterich, J. H. & D. E. Smith. (2009). "Nonplanar Faults: Mechanism o slip and off-fault Damage." Pure and Applied Geophysics **166**: 1799-1815.

Dunham E. M., D. Belanger, L. Cong, & J. E. Kozdon. (2011). “Earthquake Ruptures with Strongly Rate-Weakening Friction and Off-Fault Plasticity,Part 2: Nonplanar Faults.” Bulletin of the Seismological Society of America, **101**(5): 2308–2322.

Fairhurst, C. (1964), ”On the validity of the ‘Brazilian’ test for brittle materials” International Journal of Rock Mechanics and Mining Sciences & Geomechanics Abstracts **1**(4): 535-546.

George B. Arfken and H. J. Weber. (2001) Mathematical Methods for Physicists. Harcourt: San Diego.

Jaeger, J. C., N. G. W. Cook, & R. W. Zimmerman. (2007), Fundamentals of rock mechanics, Wiley-Blackwell.

Mandelbrot, B. B., D. F. Passoja, & A. J. Paullay (1984). "Fractal character of fracture surfaces of metals," Nature **308**: 721–723.

Ohanaka, M. (2004). "A Constitutive Scaling Law or Shear Rupture that is Inherently Scale Dependent, and Physical Scaling of Nucleation Time to Critical Point." Pure and Applied Geophysics **161**: 1915-1929.

Patton, F. D. (1966). "Multiple Modes of Shear Failure in Rock." International Society for Rock Mechanics **Lisbon 1**: 509-513.

Persson, B. N. J. (2006). "Contact Mechanics for Randomly Rough Surfaces." Surface Science Report **61**: 201-227.

Press, W. H., S. A. Teukolsky, W. T. Vetterling, & B. P. Flannery (2007), Numerical Recipes: The Art of Scientific Computing. 3rd edition, Cambridge University Press, New York.

Power, W. L., & T. E. Tullis (1991). "Euclidean and fractal models for the description of rock surface-roughness" Journal of Geophysical Research **96**(B1): 415-424.

Power, W. L., T. E. Tullis & Weeks (1988) "Roughness and wear during brittle faulting" Journal of Geophysical Research **93**(15): 268-15,278.

Power, W. L., T. E. Tullis, S. R. Brown, G. N. Boitnott, and C. H. Scholz (1987) "Roughness of natural fault surfaces" Geophysics Research Letters **14**: 29-32.

Queener, C. A., T. C. Smith & W. L. Mitchell (1965). "Transient wear of machine parts" Wear **8**: 391-400.

Renard, F., C. Voisin, D. Marsan, & J. Schmittbuhl (2006), "High resolution 3D laser scanner measurements of a strike-slip fault quantify its morphological anisotropy at all scales." Geophysics Research Letters **33**: L04305, 10.1029/2005GL025038.

Renard, F., K. Mair & O. Gundersen (2012), "Surface roughness evolution on experimentally simulated faults." Journal of Structural Geology **45:** 101-112.

Sagy, A., E. E. Brodsky & G. J. Axen,. (2007). "Evolution of Fault-Surface Roughness with Slip." Geology **3**: 283-286.

Sagy, A. & E. E. Brodsky (2009a). "Geometric and Rheological Asperities in an Exposed Fault Zone." Journal of Geophysical Research **114**(B023101): 10.1029/2008JB005701.

Sagy, A. & E. E. Brodsky (2009b). "Constraints on Faulting Mechanism Using 3D Measurements of Natural Faults."in: Y. H. Hatzor., J. Sulem, I. Vardoulakis, (Eds.), Meso-Scale Shear Physics Earthquake and Landslide Mechanics, 117 – 122.

Scholtz H. (2002). "The Mechanism of Earthquakes and faulting." ISBN 0-521-65223-5.

Segall, P. & D.D. Pollard (1983). "Nucleation and growth of strike slip faults in granite" Journal of Geophysical Research 88(B1): 555-568.

Tisato, N., G. Di Toro., N. De Rossi., M. Quaresimin. & T. Candela (2012). "Experimental investigation of flash weakening in limestone." Journal of Structural Geology **38**: 183-199.

Wang, W. B., and C. H. Scholz (1994). "Wear processes during frictional sliding of rock - a theoretical and experimental-study" Journal Geophysics Research **99**: 6789-6799.